Chemical Geology 683 (2025) 122753

Contents lists available at ScienceDirect

Chemical Geology

journal homepage: www.elsevier.com/locate/chemgeo

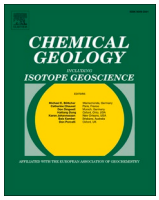

Research Paper

Widespread chemically oscillating reactions during oxidative organic diagenesis recorded during the Ediacaran

Dominic Papineau [a,b,*], Zhenbing She [b], Liangxuan Jiao [c], Shuzhan Liu [d], Deng Liu [b], Genming Luo [b], Chao Li [c]

[a] Institute of Deep-Sea Science and Engineering, Chinese Academy of Sciences, Sanya 572000, China
[b] State Key Laboratory of Biogeology and Environmental Geology & School of Earth Sciences, China University of Geosciences, Wuhan, China
[c] State Key Laboratory of Oil and Gas Reservoir Geology and Exploitation, Institute of Sedimentary Geology, Key Laboratory of Deep-time Geography and Environment Reconstruction and Applications of Ministry of Natural Resources, Chengdu University of Technology, Chengdu 610059, China
[d] Wuhan Centre, China Geological Survey, Wuhan, China

ARTICLE INFO

Editor: Vasileios Mavromatis

Keywords:
Concretion
Granule
Botryoid
Diagenesis
Organic matter
Ediacaran
Abiotic decarboxylation
Belousov-Zhabotinsky reaction

ABSTRACT

The Neoproterozoic oxygenation event co-occurred with widespread phosphate deposition in sediments, the formation of concretionary structures, perturbations in stable carbon and sulphur isotope compositions, and possibly with the emergence of animals, all well-recorded in South China. However, the significance of concretionary structures in this context remains enigmatic. Occurrences of fossils inside Ediacaran apatite granules are also poorly explained by rounding through sediment reworking, which is the model usually invoke the origin of granules. The main problem with the reworking model is that it does not predict that granules should contain specific minerals, geometric patterns, or fossils. Here we show that concretionary diagenetic spheroids such as botryoids, rosettes, granules, nodules, and concretions are widespread in the Ediacaran Doushantuo Fm and we compare their patterns and composition to those involved in chemically oscillating reactions (COR). We report that diagenetic spheroids in the Doushantuo Fm have distinct radial, concentric, twinned, and cavity-like patterns and geometries that span several orders of dimension sizes. Their mineral assemblage is documented to be variably dominated by a small range of minerals including apatite, carbonate, chert, and sulphide. Their ubiquitous content of redox sensitive trace elements and halogens shows that they contain some residual reactants from their original sedimentary environments. The organic matter (OM) therein includes more than six different types of crystallinities and disorder, which is interpreted to suggest variable abundance of molecular functional groups from biomass decomposition or low-grade metamorphism. Hence, Doushantuo diagenetic spheroids have self-similar geometric patterns and, combined with their mineralogy, trace elements, and diverse OM, they are comparable to compounds involved in pattern formation during new COR experiments reported here. The COR model therefore points to diagenetic spheroids as a continuum of fractal objects and patterns, which is argued to have formed during the diagenetic decarboxylation of carboxylic acids from biomass, although carboxylic acids on other planetary bodies could also be abiotic in origin. The abiotic COR model is not inconsistent with previous models for the origin of diagenetic spheroids, but it is more specific in explaining their patterns, mineralogy, and content of OM and fossils. Hence, COR should be considered as a major geochemical process involved in the formation of diagenetic spheroids in the Doushantuo Fm, which represents a new model to understand abiotic carbon cycling during diagenesis, and which is also applicable to extraterrestrial settings.

1. Introduction to chemically oscillating reactions and diagenetic spheroids

The physical phenomenon of chemically oscillating reactions (COR) has been proposed to produce self-similar patterns in diagenetic spheroids documented in chert (Papineau et al., 2017, 2021; Varkouhi et al., 2022; Varkouhi and Papineau, 2023), jasper (Dodd et al., 2017, 2018; Papineau et al., 2022), phosphorite (Papineau et al., 2016), and

* Corresponding author at: Institute of Deep-Sea Science and Engineering, Chinese Academy of Sciences, Sanya 572000, China.
E-mail address: dpapineau@idsse.ac.cn (D. Papineau).

https://doi.org/10.1016/j.chemgeo.2025.122753
Received 25 November 2024; Received in revised form 19 March 2025; Accepted 20 March 2025
Available online 28 March 2025

carbonate (Papineau, 2020; Gabriel et al., 2021; Goodwin and Papineau, 2022). The COR model has also been invoked in the context of patterns in sedimentary concretions and agate geodes (Papineau, 2024). Overall, COR represent spontaneous, abiotic, and redox reactions that are likely important for the global carbon cycle and for the formation of various objects in a range of chemical and clastic sedimentary rocks. The most notable aspect of COR is their incipient production of characteristic patterns of circular concentricity, colour gradients, radially diffusing waves, and characteristic circular twins when the waves destructively interfere, which in turn produces cavity shapes. The classical COR is the Belousov-Zhabotinsky (B-Z) reaction, discovered in the late 1950's by Boris Belousov (Belousov, 1958 – cited in Belmonte et al., 1997), but COR is only broadly recognised since 1970 (Zaikin and Zhabotinsky, 1970). The classical COR involves malonic acid [$C_3H_4O_4$], sulphuric acid [H_2SO_4], bromate [BrO_3^{-1}], bromide [Br^{-1}] and ferroin [phenanthroline ferrous sulphate], which is a redox-sensitive colour indicator that causes self-catalysis of the reaction and enables contrasting colours to be visualised as the reaction unravels. In general, during COR, malonic acid and other carboxylic acids are decarboxylated (i.e. losing their -COOH groups) under the combined influence of bromide, strong acids, strong oxidants, and redox-sensitive iron. Various other reactants can also replace the above ones used in the classical Belousov-Zhabotinsky reaction (Belmonte et al., 1997). As a result, COR in thin films produce CO_2 as well as characteristic oscillations of self-similar, circularly concentric patterns that diffuse radially from randomly located oxidation spots. This is akin to concentric and radial patterns displayed by diagenetic spheroids in sedimentary rocks.

Phosphorite, jasper, and chert deposits commonly contain spheroidal concretionary objects that record important diagenetic processes. These objects include concretions, nodules, granules, rosettes, and botryoids, which can all be grouped as 'diagenetic spheroids'. This term is adopted here, as before by our group, because all these objects are linked by several unifying facts: 1) they all have an origin strongly influenced by abiotic diagenetic processes (Marshall and Pirrie, 2013; Papineau et al., 2016; Cui et al., 2018; Varkouhi et al., 2022), 2) they commonly have circularly concentric and radially aligned mineral patterns (Coleman, 1993; Papineau et al., 2016; Dodd et al., 2018; Varkouhi and Papineau, 2023), 3) their mineral composition is dominated by either chert, carbonate, phosphate, and/or sulphide (Seilacher, 2001; She et al., 2014; Papineau et al., 2017; Papineau, 2020), and 4) they are most commonly associated with fossils and/or organic matter (OM) (Seilacher, 2001; Marshall and Pirrie, 2013; She et al., 2014; Plet et al., 2016; Papineau et al., 2017). Most current models for the origin of diagenetic spheroids contend that their formation occurs through nucleation processes around a central object (e.g. Fouke, 2011), secondary diagenetic replacement of primary minerals (e.g. Maliva et al., 2005), and/or rounding by wave-action and reworking of detrital sediments (e.g. Hiatt et al., 2015). However, these commonly proposed formation models do not properly explain why diagenetic spheroids should have specific internal geometric mineral patterns, nor why they should be composed of a limited range of dominant minerals, nor why they should be commonly associated with fossils or OM. Hence, the exact formation process involved in different types of diagenetic spheroids in the geological record remains uncertain and enigmatic to some extent, which translates into several currently outstanding problems in geology, and particularly in geochemistry, mineralogy, sedimentology, and exobiology.

Hence, a brief review is presented for the proposed origin of concretions, nodules, granules, rosettes, and botryoids. Firstly, the growth of concretions and nodules (> 10 mm in size) is usually interpreted to involve the microbially-mediated decomposition of biomass during diagenesis (Irwin et al., 1977; Xiao et al., 2010) and abiotic physical-chemical processes (Berner, 1968; Seilacher, 2001). However, these growth models do not specifically predict why concretions and nodules should commonly contain mineral patterns with circular concentricity and radial geometry.

Secondly, granules are smaller than concretions and nodules and are here taken to be ca. 0.2 to 10 mm in size based on observations from the Doushantuo phosphorites (see below). This is slightly different from their size range (2.0 to 4.0 mm) defined on the Wentworth scale, based on the poorly justified assumption that they are detrital particles, which is not adopted here because granules can be smaller or larger and their origin could be diagenetic (Papineau et al., 2017; Dodd et al., 2018). Granules are spheroids whose formation is typically attributed to wave-action or sedimentary re-working thought to cause detrital particles or precipitates to become rounded on sedimentary hardgrounds (Simonson, 1985). Granule formation has also been interpreted as a combination of processes involving redox-aggradation, unconformity-bound rounding, and biomass decomposition (Pufahl and Grimm, 2003 – they are called "phosphate coated grains" therein). Unfortunately, models proposed so far for granule formation do not easily explain mineral patterns with circularly concentric and radial geometries, their limited range of dominant minerals, and their common contents of OM and microfossils. Hence, assumptions in formation models highlight the need to document a greater diversity of minerals and patterns to further test formation models for granules.

Thirdly, rosettes (ca. 0.005 to 0.2 mm in diameter) also involve diagenetic processes as demonstrated by laboratory diagenesis experiments using OM or microbial biomass as a reactant to produce microscopic rosettes of apatite (Blake et al., 1998), siderite [$FeCO_3$] (Köhler et al., 2013), and proto-dolomite [$CaMg(CO_3)_2$] (Liu et al., 2019). However, the best-known rosettes are 'pyrite framboids', which are rounded and may co-occur with marcasite [FeS_2], such that these pyrite-marcasite rosettes display radial and circularly concentric patterns (Schieber, 2007). The common abundance of OM in rocks with pyrite framboids suggests a genetic link between OM and their formation process. Diagenetic pyrite framboids are also common inside carbonate concretions, where they have been considered a precursor to outward diffusion of later diagenetic pyrite found in concretion rims (Coleman and Raiswell, 1995). Lastly pyrite framboids sulphur isotope composition and variable diameter are considered to reflect paleo-environmental redox conditions (Gorjan et al., 2007; She et al., 2016). Overall, while microscopic rosettes are commonly considered diagenetic in origin, there lacks a comprehensive model to explain their formation in nature, and which can also specifically predict their limited range of mineral composition, their patterns, as well as their common association with OM, fossils, and other diagenetic spheroids.

Fourth and lastly, botryoids are usually known to span sizes from sub-millimetre to decimetre and represent a mineral habit adopted by a range of minerals that are metalliferous, hydrated, alkaline, phosphatic, or carbonated. The two minerals that most commonly adopt a botryoidal habit are quartz and malachite, both of which always have radially aligned acicular crystals that display circularly concentric colour gradients and spheroidal twins (Papineau, 2020; Papineau et al., 2021). It has been suggested that geometric patterns in botryoidal minerals grow heterogeneously as a function of time, and that they can be influenced by external processes triggering nucleation (Jamtveit and Hammer, 2012). Other ideas put forward to explain the periodic coloured banding in botryoids and agate geodes include the diffusion of metal cation impurities in silica gels (Liesegang, 1910) or in micritic carbonate (Hartmnan et al., 1934), and the self-organization of objects with variable crystallite size, porosity, silica phase, and colour pigments (Götze et al., 2020). However, only the recently introduced COR model predicts the formation of specific geometric patterns in botryoidal carbonate and quartz, which is supported by numerous similarities in patterns and compositions (Papineau et al., 2021; Varkouhi et al., 2022; Varkouhi and Papineau, 2023; Papineau, 2024), although it remains unclear why botryoidal minerals are associated with other diagenetic spheroids and/or fossils.

The emerging view from these observations of compositions and patterns in various types of diagenetic spheroids is that they may form from the same kind of diagenetic reactions during biomass decomposition and mineralization. In this work, the COR model is tested to explain

the origin of both patterns and substances in diagenetic spheroids, which has been described as a robust approach to search for biosignatures of extra-terrestrial life (Chan et al., 2019). This work also addresses specific questions such as: Could COR shed light on the origin of widespread occurrences of diagenetic spheroids during the Ediacaran? Might COR also explain the exceptionally preserved fossils commonly found within diagenetic spheroids? In particular, the Ediacaran Doushantuo Fm is known to host a wide range of diagenetic spheroids including some associated with exceptional fossils of early complex multicellular life, and most notably, the oldest purported fossil animal embryos (i.e. fertilised eggs) and some of the oldest fossil algae (Xiao et al., 1998), although these interpretations are debated for their affinity to modern relatives (Moczydłowska and Liu, 2021). This investigation is thus focused on the diversity of patterns and compositions in diagenetic spheroids from the Doushantuo Fm.

2. Geological setting of the Doushantuo Formation for the studied samples

The Doushantuo Fm in South China (Fig. 1) preserves a world-class record of post-Snowball Earth sedimentation with major economic phosphate deposits commonly with spheroidal concretionary structures (Cook and Shergold, 1984). The Doushantuo Fm accumulated between 635 and 551 Ma (Condon et al., 2005) and other age constraints include 599 Ma apatite from Member II near Yichang (Barfod et al., 2002), as well as 612 Ma from the bottom of unit 5 near Weng'an (Yang et al., 2021). There are four lithostratigraphic members in the Doushantuo Fm in the Yichang area: Member I comprises ^{13}C-depleted cap carbonate, Member II is dominated by ^{13}C-enriched carbonates, black shales, and widespread phosphorite, Member III is dominated by ^{13}C-depleted carbonate rocks, and Member IV comprises organic-rich black shales in which $\delta^{13}C_{carb}$ values are negative, but recover to become positive near the boundary with the overlying Denying Fm (Jiang et al., 2007, 2011; McFadden et al., 2008; Li et al., 2010; Wang et al., 2008). These secular carbonate carbon isotope trends in the area around Yichang in South China have been used to propose chemostratigraphic correlations with other Ediacaran sequences worldwide (Zhou and Xiao, 2007; Jiang et al., 2007). Furthermore, carbon isotope excursion along with nitrogen isotope systematics have been used to guide interpretations on the variable influence of primary and secondary productivity in the Ediacaran Ocean (Ader et al., 2009; Wang et al., 2018; Cañadas et al., 2022). In the stratigraphy of the Doushantuo Fm (Fig. 2A), there are many phosphatic and organic-rich sedimentary rocks with diagenetic spheroids (Fig. 2B). Diagenetic spheroids are widespread in the whole Doushantuo Fm, however they are also progressively less common in the following range of paleoenvironments: in the inner shelf and intrashelf basin (near the cities/towns of Xiaofenghe, Jiulongwan, Yichang, Baizhu, and Zhongxiang), outer shelf (Zhongling, Yangjiaping, Weng'an, Beidoushan, and Duoding), and slope and basin (Tianping, Siduping, and Wuhe) paleoenvironments (Fig. 1, 2B) (Jiang et al., 2011; Zhu et al., 2013). This work is focused on samples collected from three main localities with excellent outcrop exposures of Member II near the cities of Weng'an, Yichang, and Zhongxiang (Fig. 1).

Samples investigated in this work (Table 1) come from phosphorite mines in the Baiyan anticline at Weng'an in Guizhou Province and include drill cores (*ZK511*, *ZK115*, *ZK701*, and *ZK703*; She et al., 2016; Jiao et al., 2023b) and outcrop samples (*DO1706*, *16DT01C*; Papineau et al., 2021). Samples also come from outcrops along road cuts, mining pits, and mining tunnels in the Three Gorges area of Hubei Province and include samples from the Jiulongwan section (*YG18*-series, *11YC10–1*; Papineau et al., 2021), as well as from the areas around Yichang (*TP09*-series; She et al., 2013, 2014), Zhongxiang (*13ZX*-series), and Baizhu (*12BK10–14*). All these samples are selected from a larger collection of samples, because they contain diagenetic spheroids and are available as polished thin sections. The diagenetic spheroids investigated in this work also represent the four lithostratigraphic members of the Doushantuo Fm (henceforth, Member I to IV; Fig. 2A), and there is a focus on occurrences of phosphorite from Member II, which is selected based on its association with apatite granules (Table 1) and variably sized patterns in mineralised circularly concentric objects seen in outcrops and in

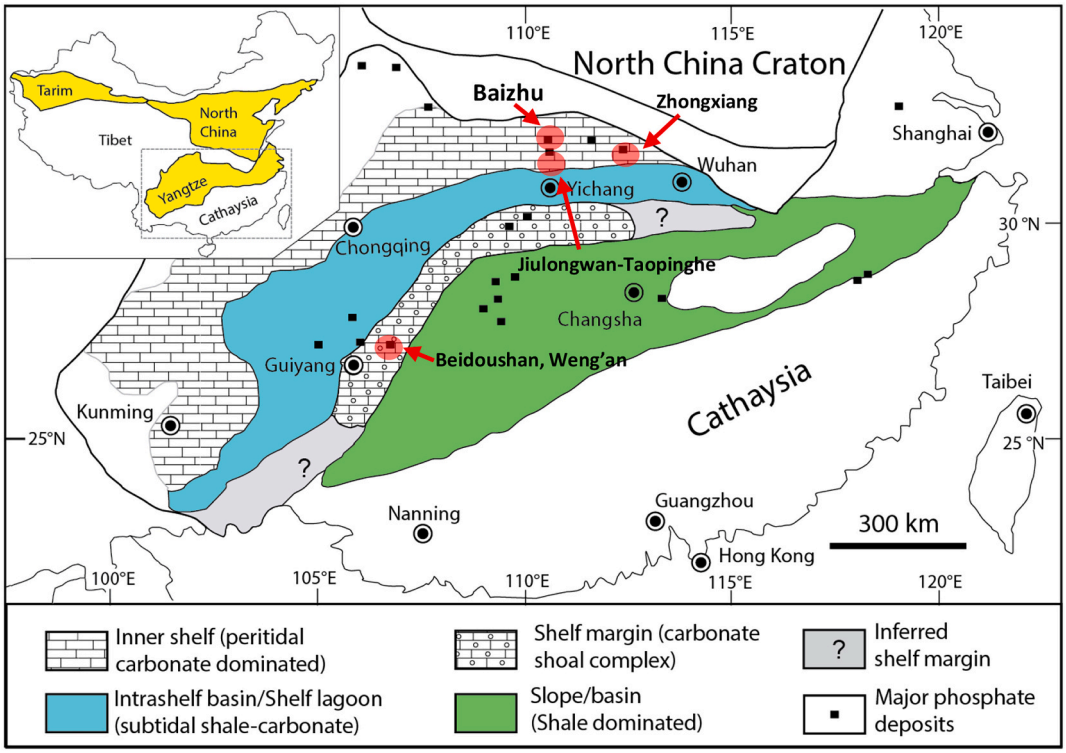

Fig. 1. Geological context of the studied Doushantuo specimens. Geological formations with locations studied in this work shown with red dots (modified after She et al., 2014). (For interpretation of the references to colour in this figure legend, the reader is referred to the web version of this article.)

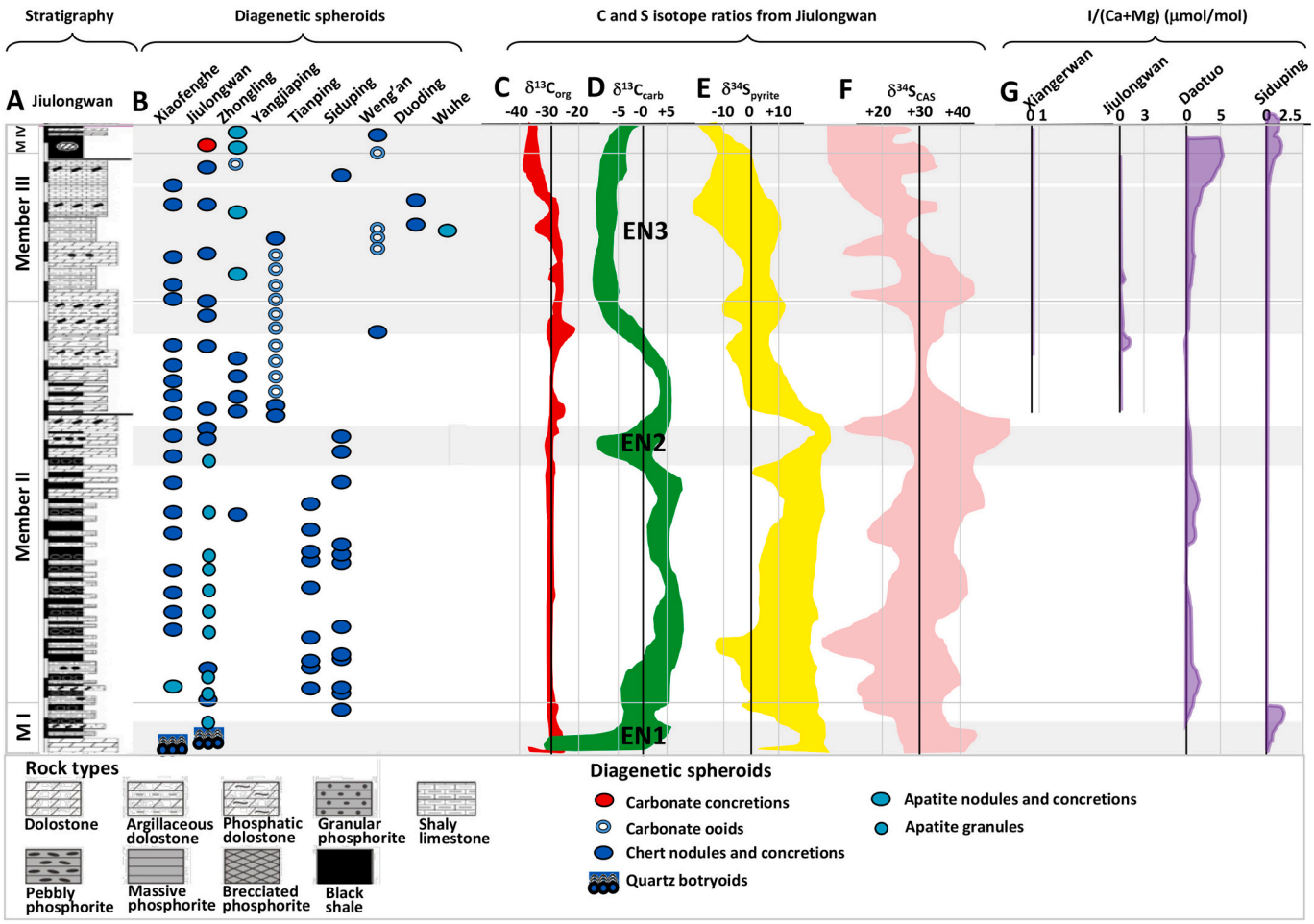

Fig. 2. Stratigraphic correlations of beds with diagenetic spheroids in the Doushantuo Formation plotted in the context of selected published chemostratigraphic profiles. From left to right, the columns show (A) the stratigraphy of the Jiulongwan section (modified from Jiang et al., 2011), (B) the sequence of diagenetic spheroids structures composed of quartz, apatite, and carbonate (modified from Jiang et al., 2011), (C—D) Correlations of carbon isotope profiles for organic matter and carbonate for the Jiulongwan section (the latter is used to define the 'excursions negatives' (EN1–3)) (McFadden et al., 2008), (E-F) the sulphur isotope profiles of pyrite and carbonate-associated sulfate (CAS) at Jiulongwan (McFadden et al., 2008), and (G) iodine concentration normalized to Ca + Mg concentration (in mmol/mol) as a proxy for seawater iodate (Wei et al., 2019).

thin sections (Figs. 3 and 4). This work builds on previous studies on these Doushantuo sample suites to understand the Ediacaran phosphorous cycle. Previous studies include investigations into the composition and architecture of microbial community in granular phosphorites (She et al., 2013, 2014), the sedimentology of phosphorites (She et al., 2013; Jiao et al., 2023b) and the characteristics of botryoidal to concretionary chert (Papineau et al., 2021). Additionally, research on oxidative diagenesis in environments containing glauconitic, pyritiferous, or bedded phosphorites has provided significant insights (She et al., 2016; Algabri et al., 2020; Jiao et al., 2023a).

Sedimentary carbonates from these studied localities are known to also preserve unusual perturbations in carbon isotopes, as seen for instance with secular ^{13}C-depleted carbon isotopes in three negative excursions (EN1-EN3) in both organic matter and carbonate minerals in the Jiulongwan area (Fig. 2C-D) (Jiang et al., 2007; Zhou and Xiao, 2007; McFadden et al., 2008), in the Zhongxiang area (Zhu et al., 2013), and in the Weng'an area (Zhou and Xiao, 2007). Occurrences of diagenetic spheroids do not exactly follow these post-glacial negative isotope excursions in carbonates, however they are mineralogically varied and are widespread throughout the four Doushantuo members near Yichang (Fig. 2B) (Jiang et al., 2011; Zhu et al., 2013) and the four lower units of the Doushantuo Fm near Weng'an (Xiao et al., 2014; She et al., 2016). To explain the unusual carbonate isotope signals, possible interpretations include the oxidation of marine OM, a large reservoir of dissolved organic carbon in the water column, the diagenetic oxidation of OM in sediments, hydrothermal alteration, and a changing methane cycle after sediment burial (Jiang et al., 2003; Wang et al., 2008; Bristow et al., 2011; Wang et al., 2023; Dodd et al., 2023; Cañadas et al., 2024). The unusual negative carbon isotope excursions are also decoupled from isotopic variations in the sulphur cycle (McFadden et al., 2008; Muscente et al., 2015) as evidenced by highly variable sulphur isotopic composition in pyrite and carbonate associated sulphate (Fig. 2E-F) (McFadden et al., 2008; Li et al., 2010), in pyrite rosettes (Cui et al., 2018), and in chert nodules (Xiao et al., 2010). Therefore, both the origins of negative carbonate carbon isotope excursions and of diagenetic spheroids remain uncertain and highly debated. Furthermore, these sedimentological features are not currently comprehensively integrated into the unravelling Ediacaran story of post-glacial oxygenation and deoxygenation (Jiang et al., 2011; Zhu et al., 2013; Muscente et al., 2015).

3. Analytical methods

3.1. Optical microscopy

Optical microscopy was performed to identify targets of interest in more than sixty polished thin sections of botryoidal quartz and granular phosphorite specimens from South China (listed in Table 1). Thin

Table 1
Main specimens and their locations studied in this work.

Sample name	Latitude & longitude	Locality and stratigraphy*	Rock type
Outcrop samples			
YG1801a&b	N: 30°80701 E:111°067824	Jiulongwan section, Yichang, Member I	Botryoidal quartz and carbonate
YG1803	N: 30°80701; E:111°067824 (about 50 m up the road from YG1801)	Jiulongwan section, Yichang, Member II	Chert concretion in black phosphatic shale
DO1706	N: 27°01′10.7″ E:107°23′20.9″	Beidoushan, Weng'an unit I	Botryoidal quartz and carbonate
TP0901–02	N: 31°16′26.4″ E:111°16′23.6″ (from Ph1 3–3 bed)	Yichang, Member II	Granular phosphorite, fossiliferous
16DT01C	N: 27°1′43″ E: 107°23′39″	Datang, Unit II	Banded barite and dolostone rock
13ZX1–6	N: 31°13′36″ E: 112°24′50″ Base of Ph1, mining tunnel	Zhongxiang, Member II	Concretionary phosphorite
13ZX2-5B	N: 31°26′02″ E: 112°16′10″ mining tunnel	Zhongxiang, Member II	Concretionary phosphorite
12BK10–14	N: 31°40′53″ E: 110°56′20″ mining pit	Baizhu, Member II	Granular phosphorite, fossiliferous
11YC10–1	N: 30°48′08″ E: 110°03′19″ Road-cut outcrop	Jiulongwan section, Yichang, Member II (base)	Black shale with chert concretions
Drill core samples			
ZK511–15	N: 27°2′31″ E: 107°24′15″	Weng'an, Unit II	Granular phosphorite, fossiliferous
ZK511–12	N: 27°2′31″ E: 107°24′15″	Weng'an, Unit II	Granular phosphorite, fossiliferous
ZK511–32	N: 27°2′31″ E: 107°24′15″	Weng'an, Unit IVB	Granular phosphorite, fossiliferous
ZK511–33	N: 27°2′31″ E: 107°24′15″	Weng'an, Unit IVB	Granular phosphorite, fossiliferous
ZK115–22	N: 24°4′45″ E: 107°24′25″	Weng'an, Unit II	Granular phosphorite, fossiliferous
ZK115–33	N: 24°4′45″ E: 107°24′25″	Weng'an, Unit IVB	Granular phosphorite, fossiliferous
ZK701–6	Xinzhai, Weng'an (approximate drill core location, no GPS coordinates)	Weng'an	Stromatolitic phosphorite with intercolumnar granules
ZK703–897.46	Xinzhai, Weng'an (approximate drill core location, no GPS coordinates)	Weng'an	Concretionary botryoidal dolostone

* Stratigraphic position is reported according to Member I to IV for locations near the Three Gorges area (Jiang et al., 2007) or according to Units 1 to 5 for locations near Weng'an (Xiao et al., 2014).

sections were scanned at 1200 ppi using a regular document scanner and maps for each thin section were created. A BX-51 Olympus polarizing microscope located at University College London was used to collect plane polarised and cross polarised images as well as reflected images with the following objectives: 5×, 10×, 20×, 50×, and 100×. A condensing lens was used for all images, but no immersion oil was applied to any thin sections, which were cleaned with an acetone wash and gentle wiping with a Kimwipe®.

3.2. Micro-Raman spectroscopy

A WITec α300 micro-Raman system (WITec GmbH, Ulm, Germany) at University College London was used to image organic matter in selected targets with circular concentricity. Micro-Raman was performed using a 532 nm laser with a power of 5–8 mW, and according to previously described techniques (Papineau et al., 2017). Briefly, an optic fiber of 50 μm in diameter is used to collect inelastically scattered photons, which were dispersed through a 600 L/mm grating, thus resulting in a spectral resolution of 4 cm^{-1}. Long-term reproducibility analyses on an internal diamond standard shows a drift of less than 1.5 cm^{-1} for the 1335 cm^{-1} peak for diamond. The spatial resolution was set at three pixels per micrometre, whereas the acquisition time on each pixel was 0.6 s. Hyperspectral images were created using a colour code corresponding to the strongest unique peak of all phases present: carbonate in green (filter centre = 1090 cm^{-1}, width = 20 cm^{-1}), quartz in blue (filter centre = 465 cm^{-1}, width = 30 cm^{-1}), apatite in turquoise (filter centre = 965 cm^{-1}, width = 20 cm^{-1}), pyrite in yellow (filter centre = 343 cm^{-1}, width = 25 cm^{-1}), marcasite in turquoise (filter centre = 314 cm^{-1}, width = 25 cm^{-1}), anatase in pink (filter centre = 143 cm^{-1}, width = 25 cm^{-1}), rutile in purple (filter centre = 660 cm^{-1}, width = 40 cm^{-1}), barite in white (filter centre = 992 cm^{-1}, width = 20 cm^{-1}), feldspar in purple (filter centre = 515 cm^{-1}, width = 20 cm^{-1}), organic matter in red (filter centre = 1590 to 1605 cm^{-1}, width = 70 cm^{-1}).

3.3. Rock powder preparation

Powders of diagenetic spheroids were prepared to obtain bulk elemental compositions of major, minor, and trace elements. They were generated using a steel mortar and pestle, previously cleaned using soap and brush, DI water rinses, acetone rinse, muffled quartz crushing to very fine powder, rinsed with DI water and air dried. Powders were transferred to muffled clear borosilicate glass vials (two hours at 600 °C). Plastic caps were soaked in 10 % HCl for 24 h, followed by three DI water rinses and air drying.

3.4. Bulk elemental analyses by ICP-MS and ICP-OES

For bulk analysis of trace elements, ~0.1 g of powder was initially heated in a mixture of 1.0 ml hydrochloric acid (37 % wt/vol; analytical grade), 1.0 ml nitric acid (69 % wt/vol; analytical grade), and 0.5 ml hydrofluoric acid (40 % wt/vol; analytical grade) at 110 °C for 16 h. The solution was evaporated to incipient dryness before the addition of 2.0 ml HNO_3 and 0.5 ml $HClO_4$ (70 % wt/vol; analytical grade), which was again evaporated to incipient dryness. A further 1 ml aliquot of HNO_3 was evaporated and the residue dissolved in 100 ml of 1.0 % HNO_3 prior to analyses by ICP-OES and ICP-MS at University College London. ICP-OES analysis was carried out using a Varian 720-ES (Agilent, Santa Clara, California U.S.A.), whilst ICP-MS analysis was carried out using a Varian 820-MS (Agilent, Santa Clara, California, U.S.A.). All calibration standards were made via serial dilution of either single element (majors) or multi-element (REE) stock solutions supplied by Merck KGaA (Darmstadt, Germany). All data are reported as elemental in parts per million. Analyses of certified reference material NBS120c (Florida Phosphate Rock) yielded recoveries above 95 % and within about 20 % of the certified values and duplicate analyses on different ~3 cm^3 size splits from the same sample (*YG1801a* and *YG1801b*) mostly agree within 5 %.

3.5. Ion chromatography

To obtain F concentrations, sample powders were prepared by dissolving 10 mg of powder in 10 mL of 2 % nitric acid and they were subsequently manually agitated and left for ~12 h. Following centrifugation at 4000 rpm (300 s.), the supernatant was diluted 1:100 and

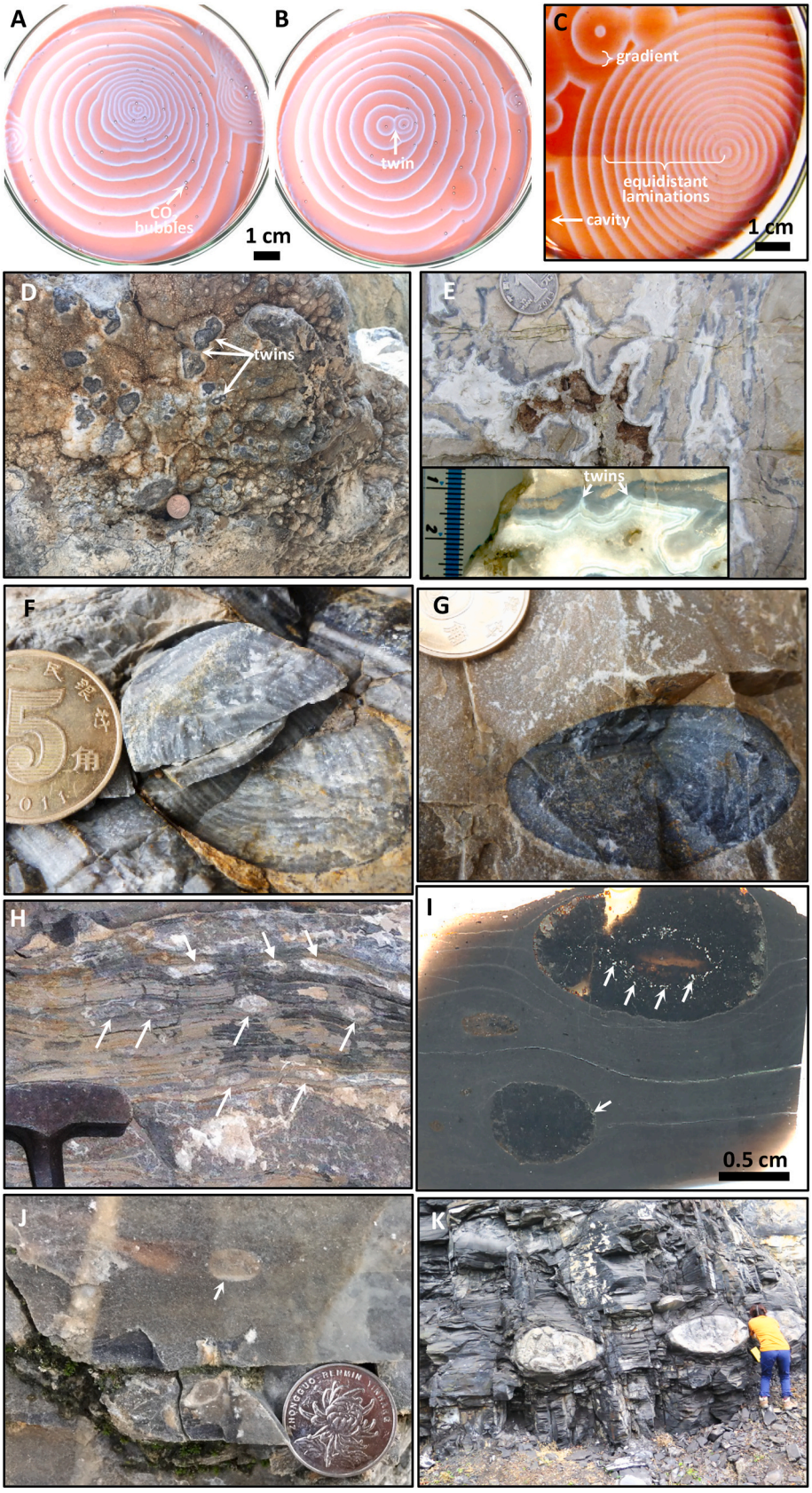

(caption on next page)

Fig. 3. Pattern comparison between COR and macroscopic botryoids and concretions in outcrops from the Doushantuo Formation. (A-C) Transmitted light images of COR in Petri dishes that produce decimetre size self-similar patterns of radially expanding patterns with concentric laminations, twins, cavities, gradients, equidistant laminations, and CO_2 bubbles. In Member I, (D) botryoidal quartz at Jiulongwan that shows spheroidal twins and (E) botryoidal 'sheeted cracks' of quartz at Beidoushan, showing spheroidal twins in inset photo of a polished slab. In Member II, (F) circularly concentric concretions of carbonate-apatite in phosphorite from Baizhu, (G) concretion of apatite in dolomite from Baizhu locality, (H) concretions of apatite (white arrows) in laminated dolomitic phosphorite from Zhongxiang, (I) finely laminated black shale with concretions of quartz rich in OM (black) and pyrite (white arrows) from Yichang (*11YC10–1)*. At Jiulongwan near Yichang, there are (J) dolomite concretions in limestone-dolostone from Member III and (K) meter-size microfossiliferous concretions of dolomite in black shale from Member IV.

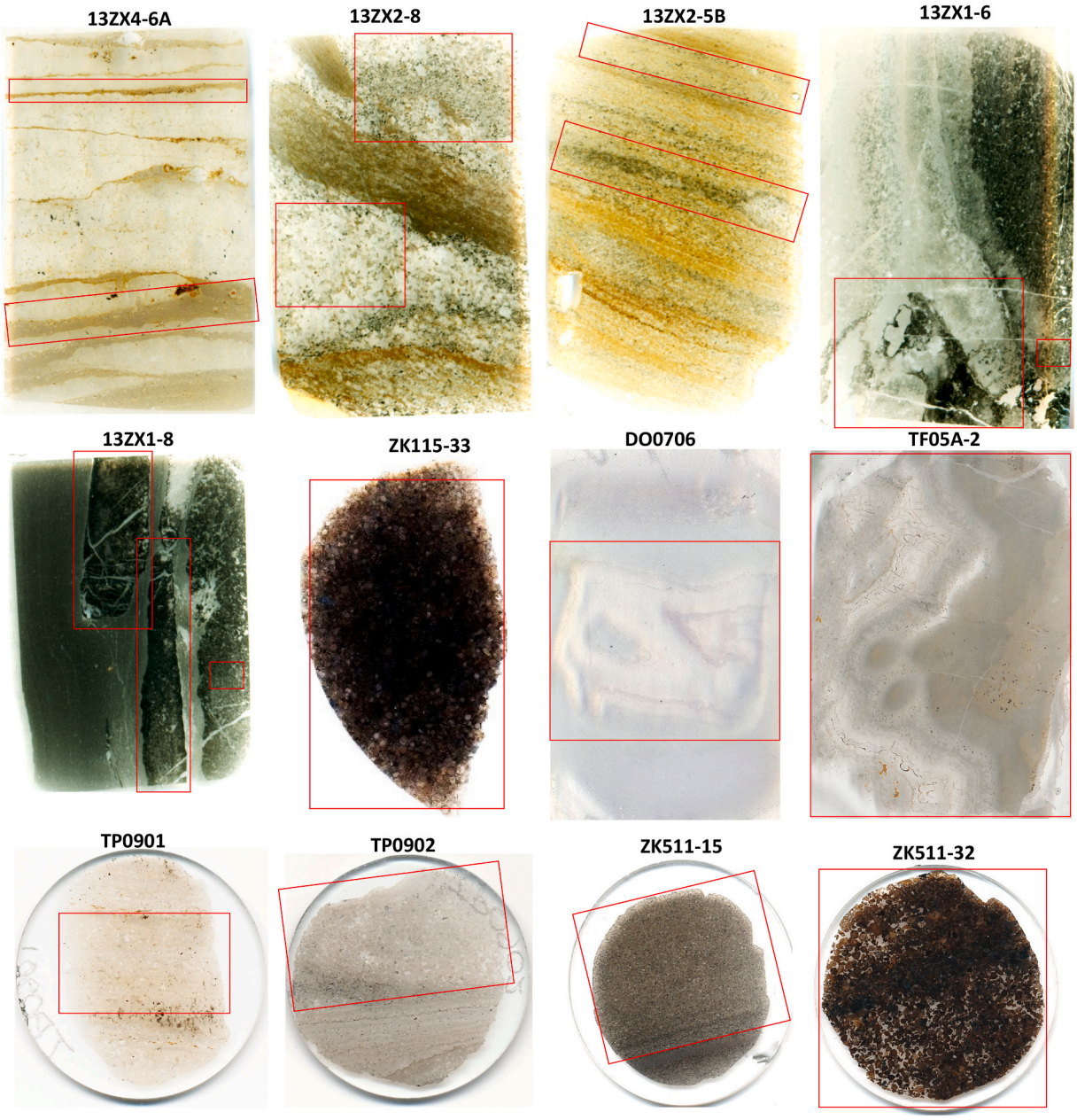

Fig. 4. Selected TL images of thin sections analyzed in this work and also showing targets in their sedimentological context. The rectangular thin sections are 2.5 cm wide and the circular ones are 2.5 cm in diameter. Red rectangles show the location of microscopic and macroscopic diagenetic spheroids in thin sections, where they occur as bands or they compose the whole rock, such as granules or botryoids. (For interpretation of the references to colour in this figure legend, the reader is referred to the web version of this article.)

transferred to 2 mL polypropylene vials prior to analysis. Selected anion analysis was performed using a Dionex™ Integrion™ HPIC™ System (Thermo, Waltham, Massachusetts, U.S.A.). The chromatography was achieved using a Dionex™ IonPac™ AS19 IC Column (4 mm) with an eluent of KOH (20 mM) generated using a EGC-KOH 500 cartridge. Flow rate was set at 0.25 ml/min, with suppressed conductivity where the voltage potential signal from the eluent is removed by suppression.

3.6. *Chemically oscillating reaction experiments*

More than 50 experiments were performed in 10 cm diameter glass Petri dishes using the following reactants: Solution A with 6 ml of (1 M)

$NaBrO_3$ mixed with (0.33 M) H_2SO_4, Solution B with 0.5 ml of (1 M) NaBr, Solution C with 1 ml of (1 M) malonic acid, 1 ml of (25 mM) ferroin (phenanthroline ferrous sulphate; Reagecon), and a drop of dilute triton X-100 (Sigma-Aldrich, St-Louis, Missouri, U.S.A.). First the solutions A and B are mixed until the yellow colour disappears, which takes approximately two minutes of gentle stirring. Then, Solution C is added along with the ferroin redox indicator and dilute triton X-100. When a homogeneously orange coloured solution is achieved by gentle stirring, the COR solution is then left still and unstirred for video footage. All experiments were performed on countertops in ambient temperatures varying between about 20 and 25 °C and on an LED-illuminated light bench. The reaction is spontaneous and out-of-equilibrium and the pattern development lasts between about 45 and 75 min, depending on the number of resets. This is because after the solution turns blue, it can be gently stirred again to become orange coloured and, when left still again, another generation of spots will begin. Data was collected using a CCD camera in both photo and video modes and only representative images are shown.

4. Results

4.1. New chemically oscillating reaction experiments

New COR experiments under standard conditions with malonic acid, bromate, bromide, sulphuric acid and ferroin successfully produce millimetre to decimetre size and oblate to perfectly circularly concentric patterns that expand radially over seconds (Zaikin and Zhabotinsky, 1970) (Fig. 3A-C). In brief, the experiments show the following: within seconds, sub-millimetre size blueish circular waves start to spontaneously and randomly appear in the orange-coloured solution of the Petri dish. Over seconds to minutes time scale afterwards, these spots diffuse radially away from the location where they first appeared and are they followed by a new generation of circularly concentric waves that starts at the same geometric centre. After about 20–30 min, the entire solution become filled with a blue colour. In summary, the pattern geometries are self-similar as they have a range of size dimensions, from 10^{-1} to 10^{-4} m, and they variably display circularly concentric waves, equidistant laminations, radial diffusion, colour gradients in laminations, circular twins, rounded asymmetry, and cavity structures among other patterns (Fig. 3A-C). Minor variations of these patterns and timings have been observed in previous experiments (Papineau et al., 2017, 2021, 2023; Papineau, 2020; Varkouhi et al., 2022; Varkouhi and Papineau, 2023). Most notably, all these self-similar patterns are akin to patterns displayed by minerals in macroscopic diagenetic spheroids from the Doushantuo Fm (Fig. 3D-K). The self-similar B-Z patterns produced in Petri dishes have at least four orders of dimension sizes (from 10^{-4} m to 10^{-1} m) (Fig. 3A-C, 5Q-U), which is a range of dimension sizes also observed in millimetric and micrometric diagenetic spheroids from the Doushantuo Fm (Figs. 5–7).

4.2. Circularly mineralised patterns in Doushantuo diagenetic spheroids

Member I is a cap carbonate that contains diagenetic spheroids as cavities lined with botryoidal quartz [SiO_2] (Fig. 3D-E) (Papineau et al., 2021). These quartz botryoids are laminated with OM gradients (i.e. brown colour gradients of concentration of disseminated OM) and form geometrically perfect, circularly concentric laminations, including with radially aligned acicular quartz (Fig. 5A-B) (see Raman image in Papineau et al., 2021). They are also associated with microscopic quartz rosettes (~50–500 μm in diameter) that display hemispherical and circularly concentric layers composed of brown gradients of concentration of OM, as well as radially aligned acicular crystals (inset in Fig. 5B). Centimetre to decimetre-size diagenetic spheroids in Member II include apatite [$Ca_5(PO_4)_3(OH,F,Cl)$] and chert [SiO_2] concretions (Fig. 3F-I), and they have circularly concentric layers of apatite, dolomite [$CaMg(CO_3)_2$], or pyrite [FeS_2] (Fig. 3F-I). In the dolomite-calcite bedded carbonate unit in Member III, there are centimetric concretions (Fig. 3J). Lastly, Member IV contains OM-rich black shale with beds of meter-size carbonate concretions that also have concentric layers (Fig. 3K). All these features have self-similar circular patterns that span at least six orders of dimension sizes (from 10^{-5} m to 10^{0} m).

The geometric patterns and fossil content of granular rocks in the Doushantuo Fm vary in colour with yellow, orange, brown, gray or black disseminated OM (Fig. 4). Our identification of OM in the studied thin sections stems from correlated micro-Raman imaging and optical microscopy extrapolated to broader areas of the same colour and patterns in thin section. Patterns in the studied diagenetic spheroids are usually composed of iron oxides and OM, commonly as the main substances that compose the circular laminations and the colour gradients. Notably, COR and diagenetic spheroids have the same twinned pattern, which occurs when two circularly concentric waves meet and their traces are erased to form cavity structures (e.g. Fig. 5S). When the traces are destructively interfered, the waves become a curvi-linear contact between the two oxidation spots, which forms twinned spheroids (i.e. with twinned acicular crystals) in isopachous apatite and quartz botryoids lined with diffused gradients of OM (Fig. 5A-B,H). Apatite granules are commonly coated with a rim of isopachous apatite with such characteristics and the intergranular space also forms cavities, which can be empty, filled with smaller spheroids (Fig. 6A-D), with some lined with OM (Fig. 5G, 6E-F), filled with apatite (Fig. 5H, 6G-H) or with OM (Fig. 5I-J). Some apatite granules also contain botryoidal patterns composed of nanoscopic pyrite and OM (Fig. 5C-D, 6I-L) or equidistant laminations of pyrite (Fig. 5J). Some rounded laminations are also asymmetric, with irregular widths that pinch and swell (Fig. 5A, G, I). Another notable feature is that apatite granules commonly contain various fossils including coccoids, filaments (Fig. 6M-N) (She et al., 2014), acritarchs (Fig. 5E-F, 6O-P) (Xiao et al., 2014), algae, and purported animal embryos (Xiao et al., 1998). Some acritarch fossils have botryoidal apatite laminations composed of OM in their cell-wall (Fig. 5E-F, 6Q), which indicates an autochthonous origin. Hence, occurrences of apatite granules with circularly concentric laminations, cavities, and botryoids, including in the cell walls of fossils, indicates a connection between circular mineralization in chemical sediments, cavities with botryoids, decomposition of biomass, and processes involved in the preservation of these fossils.

Microscopic rosettes in Doushantuo phosphorite have similar mineral assemblages including quartz, dolomite, and pyrite or marcasite as accessory minerals in granules and rosettes and in the host matrix. For instance, quartz rosettes contain circularly concentric rings of nanoscopic inclusions of marcasite and apatite (Fig. 5K-L). Circularly concentric dolomite rhombohedra can have twins as dumbbell-shaped cores as well as twinned layers of dolomite with disseminations of apatite, rutile and anatase (Fig. 5M-N, 6R-S). The latter two minerals are polymorphs of [TiO_2] commonly found with OM inside diagenetic spheroids and in fossils in older Proterozoic phosphatic chert (Papineau et al., 2017; Sirantoine et al., 2020). These concentric dolomite crystals are subhedral and they contain dumbbell structures in their centres that demonstrate a radial geometry. Lastly, pyrite rosettes and framboids are associated with dolomite and apatite as well as inclusions of OM3 to OM5, barite [$BaSO_4$], anatase, and rutile (Fig. 5O-P, 7G-I). Pyrite-marcasite rosettes best display a circular concentricity and radially aligned crystals (Fig. 7G-H), whereas pyrite framboids are more commonly twinned (Fig. 5O), comparable to similar objects reported from Cryogenian sediments (Cui et al., 2018). Such geometry is comparable to self-similar patterns in COR and the mineral composition of rosettes points to redox reactions involving abiotic sulphate reduction during biomass oxidation. To summarise, comparisons between the size range of microscopic rosettes, granules and botryoids and that of the smallest COR patterns (Fig. 5T-U) show clear and specific similarities in patterns, including 1) sub-millimetric ranges of sizes, 2) circularly concentric and equidistant laminations, 3) radial patterns analogously to the radial diffusion of chemical waves in COR, 4) twinned chemical

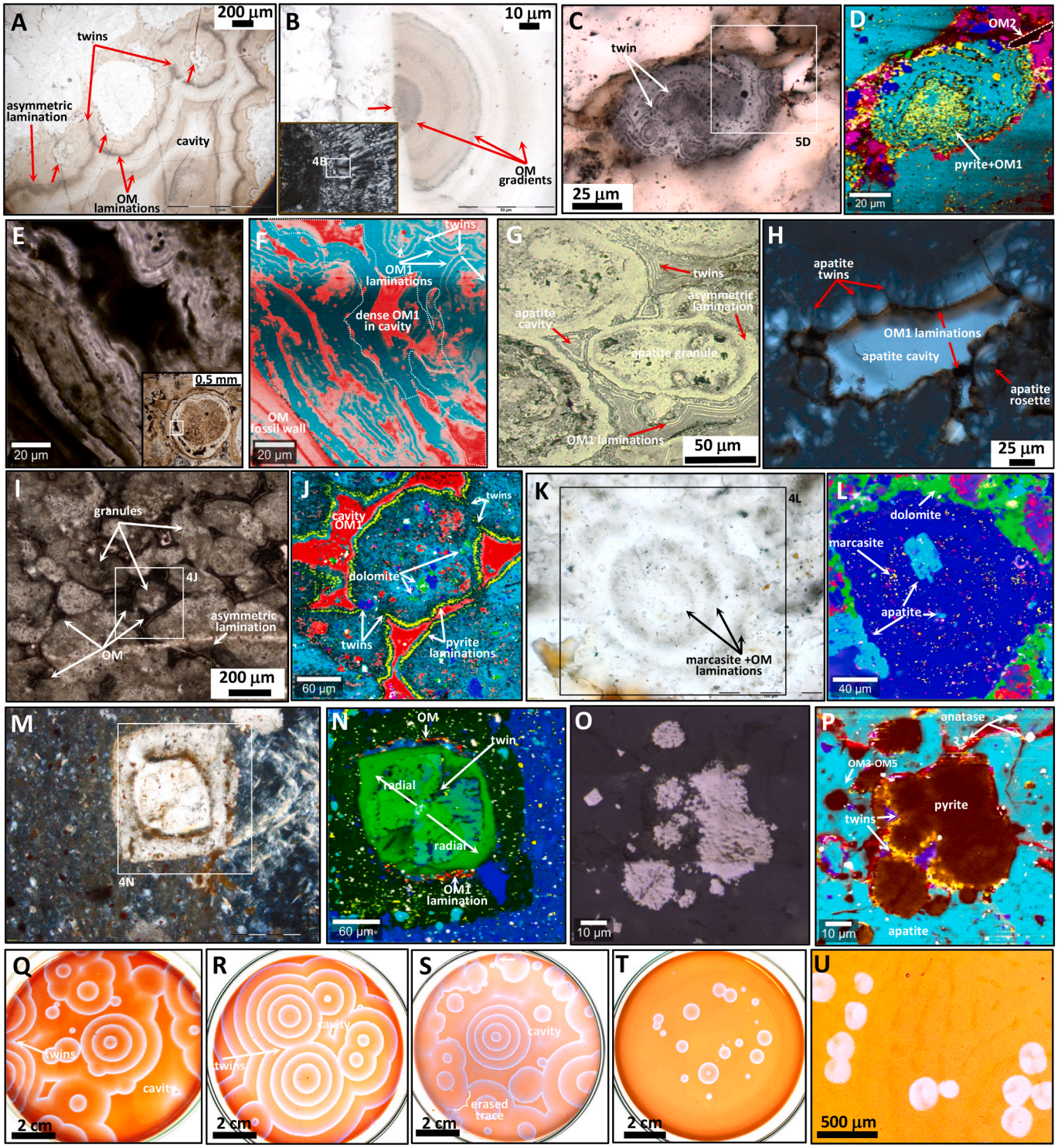

Fig. 5. Pattern comparison between COR and microscopic botryoids, granules and rosettes in the Doushantuo Formation. All these objects show radially aligned crystals and circularly concentric laminations with brown coloured OM, pyrite, or carbonate inside matrices of quartz or apatite. (A-B) TL images of quartz botryoids from the 'cap carbonate' and showing circular laminations, colour gradients, and cavity shapes all defined by OM. Asymmetric laminations have unequal width. Inset shows a CP image of radially aligned quartz (*DO1706*). (C—D) TL and Raman images of an apatite granule with pyrite and OM botryoidal laminations (*ZK511–15*); (E-F) TL and Raman botryoidal apatite with concentric laminations of OM inside an acritarch microfossil enclosing an OM-filled cavity (shown in inset) *(ZK115–33);* (G) TL image of apatite granules with concentric laminations and cavities defined by OM (*16DT01C_17*); (H) CP image of apatite with twins, cavities, and rosettes all laminated by OM (*TP0901*). (I-J) TL and Raman images of a granule with a concentric lamination of pyrite surrounded by kerogen (black) (*13ZX1–6*); (K-L) TL and Raman images of a quartz rosette with concentric laminations composed of marcasite and OM (*13ZX2-5B*). (M-N) CP and Raman images of a concentrically laminated dolomite rosette with a dumbbell shaped core that radiate in two directions (white arrows) separated by a twin plane. (O—P) RL and Raman images showing twinned, rounded pyrite framboids in concretionary apatite and associated with anatase and OM3 to OM5 (*ZK115–22*;). (Q-U) TL images of comparable COR patterns. Colours for Raman images are yellow for pyrite, red for OM, turquoise for apatite, purple for feldspar, green for dolomite, blue for quartz, and white for anatase (rutile is yellow only in (N), where there was also no pyrite). Abbreviations: TL is transmitted light, CP is crossed polars, RL is reflected light, and OM refer to organic matter of different types. (For interpretation of the references to colour in this figure legend, the reader is referred to the web version of this article.)

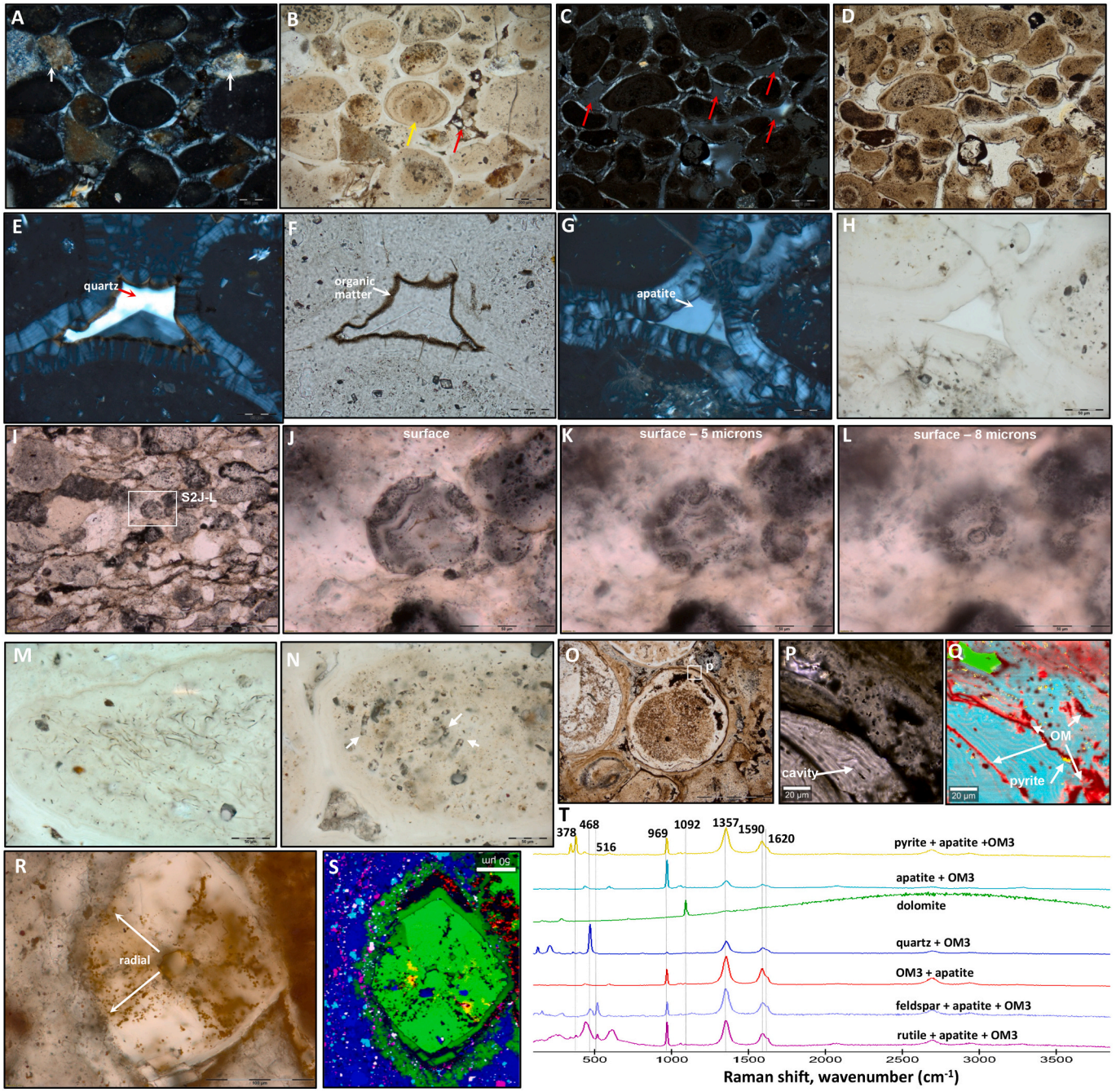

Fig. 6. Mineral patterns and composition of apatite granules from the Doushantuo Formation. (A-B) CP and TL images of concentrically laminated OM inside microfossiliferous granule (yellow arrow), cavity structure (red arrow), and diagenetic granules of sericite (white arrow), and of (C—D) diagenetic apatite granules variably rich in brown OM with empty cavities in intergranular spaces, reminiscent of botryoidal growth (now filled with epoxy – red arrows) (member II, *TP0901*, Taopinghe). (E-H) CP and Tl images of two cavities filled with quartz or apatite and laminated with OM and isopachous apatite (member II, *TP0901*, Taopinghe). I-L) TL images of a granule with botryoidal pyrite, which occurs as a cavity and circularly concentric patterns and shown in three focal planes spaced by 3 mm (member II, *ZK511–15*, Baizhu). (M-N) TL images of microfossils inside apatite granules, with isopachous apatite rims laminated with OM (member II, *TP0902*, Taopinghe). (O-Q) TL image of an acritarch microfossil and its cells wall containing botryoidal apatite laminated with OM (*ZK115–33*, member II, Weng'an). (R-T) CP with Raman image and spectra of a carbonate rosette with circularly concentric laminations of OM, radial geometry, and associated pyrite, apatite, rutile and feldspar (spectra shown in T). (For interpretation of the references to colour in this figure legend, the reader is referred to the web version of this article.)

waves, and 5) colour gradients in laminations.

4.3. Composition of Doushantuo diagenetic spheroids and crystallinity of OM

In general, Doushantuo diagenetic spheroids are typically dominated by quartz, apatite, carbonate, and pyrite, all presumably precipitated from colloidal size precursors. In addition, accessory minerals in these diagenetic spheroids can include OM, dolomite, barite, and marcasite. This is analogous with the reactants and products of COR, which can be compared, following the above order, as carboxylic acids, CO_2 bubbles, sulphuric acid and sulphate, and iron in ferroin, respectively (see section 3.6 of the analytical methods). Fluorapatite is a major mineral in granular phosphorite and a minor mineral in chert concretions from

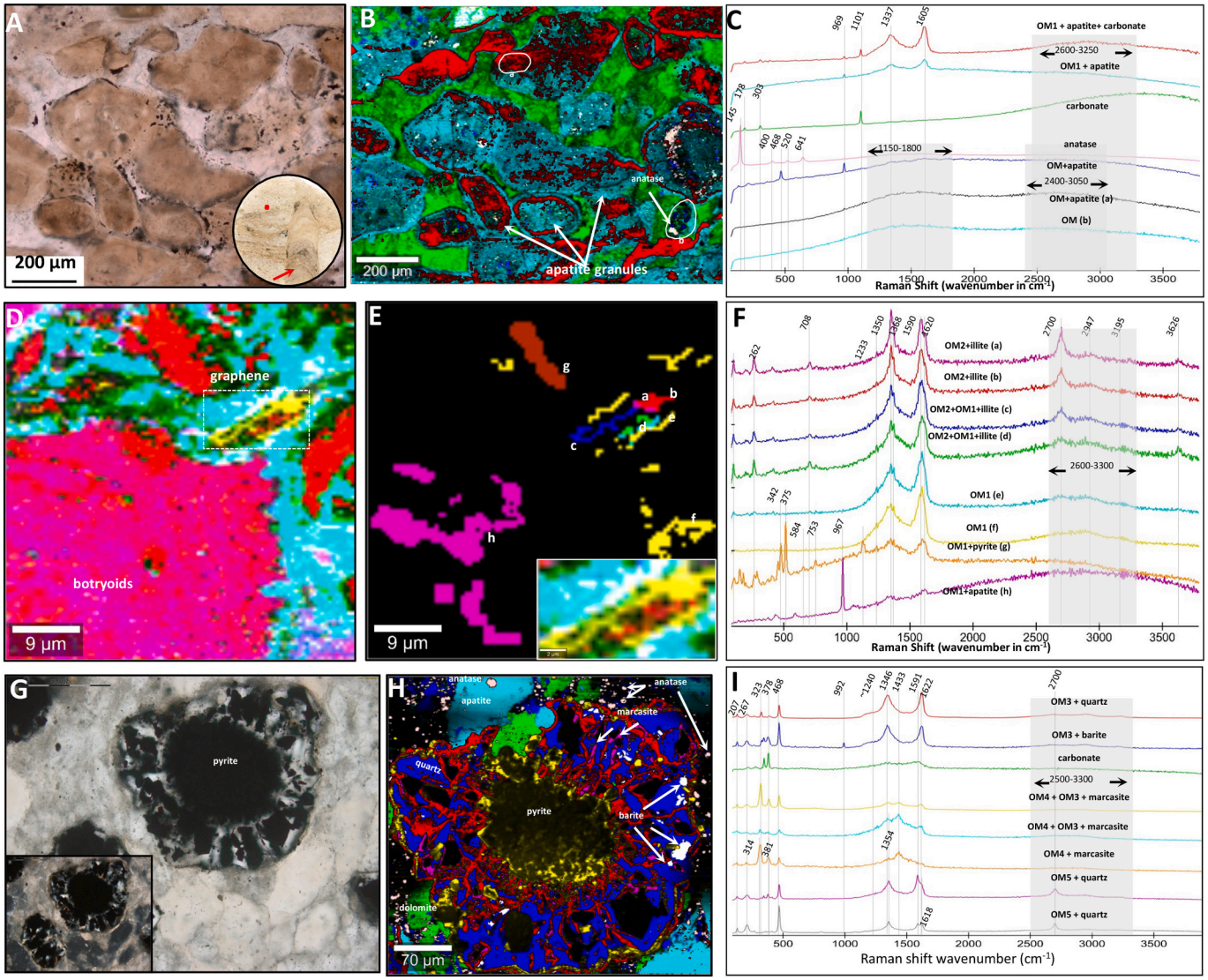

Fig. 7. Diagenetic spheroids from the Doushantuo Formation associated with variably oxidized organic matter. (A) Plane light image of sub-millimetric apatite granules rich in organic matter in dolomite matrix located (red dot in inset) between micro-digitate phosphatic stromatolite columns (red arrow in inset, which is 2.5 cm in diameter) (*ZK701–6*). (B—C) Raman image showing inclusions of quartz, anatase, and pyrite along with the correspondingly coloured spectra. (D) Raman image of apatite botryoid (from Fig. 5C-D) associated with an elongated nanoscopic fiber of graphitic carbon. (E-F) Selected areas from (D) for each of the three-end member types of OM from their Raman spectra (1, 4, 6), graphene domains. (G) Pyrite-marcasite rosette in apatite matrix (*ZK511–12*). (H) Raman image showing circularly concentric and radially aligned OM as well as inclusions of barite and titanium dioxide, and I) Raman spectra of various types of OM associated with a pyrite-marcasite rosette. (For interpretation of the references to colour in this figure legend, the reader is referred to the web version of this article.)

phosphatic black shales consistent with ppm levels of other halogens such as Br and I in these rocks from Member II (Fig. 8A; Table 2). Both botryoidal quartz from Member I and the phosphorites of Member II also have thousands of ppm of Fe (up to 4.15 %) along with hundreds of ppm Cr, Ni, and Mn, and tens of ppm of Ti, *V*, Co, Mo, and Zn (Fig. 8A; Table 2). Rare earth element (REE) profiles for these rocks are either nearly flat or slightly concave-down (Fig. 8B), and these rocks also have slightly positive Eu anomalies, small negative Ce anomalies, as well as positive Y signals (Fig. 8B).

The systematic occurrence of OM in apatite granules points to an intimate connection between diagenetic spheroids, OM, and redox reactions involving biomass. Detailed organic geochemical analyses by micro-Raman hyperspectral imaging reveal six different types of OM in microscopic apatite botryoids, granules, and concretions (compare spectra in Figs. 7, 9, and 10). Hyperspectral images of the characteristic G peak (sp^2-hybridised carbon), typically peaking at 1604 to 1608 cm^{-1}, unambiguously demonstrate that OM is distributed along laminations that constitute the concentric patterns in apatite granules (Fig. 7). Botryoidal patterns in apatite granules are usually composed of OM or pyrite. Most commonly, botryoidal patterns are associated with OM1, which is typical of kerogen with broad and strong D (for sp^3-hybridised carbon) and G peaks (Fig. 9A-B). However, OM in some botryoidal apatite-pyrite granules and pyrite-marcasite rosettes have distinct Raman spectra (Fig. 9 spectra B—C to E-J, Table 3). OM2 has narrow and strong D1 peak (ca. 1350 cm^{-1}), a narrow and strong G-peak (1590 cm^{-1}) with resolved D2 shoulder (1621 cm^{-1}), and a strong and narrow 2D peak (2701 cm^{-1}) (Fig. 7F, 9C). OM3 is also distinct with its D1 peak at 1342 cm^{-1} and D2 peak at 1622 cm^{-1}. In addition, OM associated with pyrite-marcasite rosettes (Fig. 7G-I, 9E-H) represents another, distinct type of OM – OM4 with a broad and resolved D1 peak (ca. 1349 cm^{-1}), a medium broad and strong peak at 1435 cm^{-1}, a medium broad and medium intensity D2 peak (1616 cm^{-1}), and a poorly resolved G peak around 1605 cm^{-1}. Lastly, OM5 has narrow and strong D1 and G peaks and D/G around 1 (1354 and 1591 cm^{-1}), resolved D2 peak

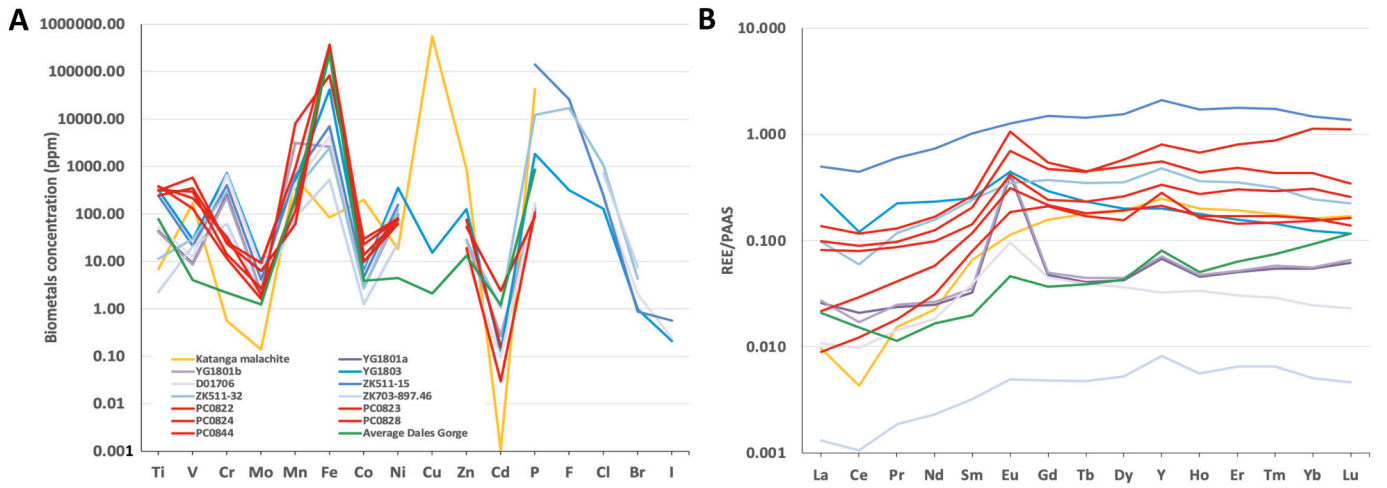

Fig. 8. Comparison of trace element trends in chemical sedimentary rocks with diagenetic spheroids. (A) Plot of the most important metals in granular and concretionary phosphorites (blue shades) and botryoidal quartz and carbonate from the Doushantuo formation (purple shades). These are compared to concretion-bearing jasper-carbonate BIF from the Eoarchean-Hadean Nuvvuagittuq Supracrustal Belt (red) (Papineau et al., 2022), the Katanga malachite (Papineau, 2020), and the average Dales Gorge BIF (green) (Konhauser et al., 2018; Pecoits et al., 2009). (B) Rare earth element plot of the same rocks, normalized to Post-Archean Australian Shales, show generally flat patterns with variably negative Ce depletions and positive Eu enrichments. (For interpretation of the references to colour in this figure legend, the reader is referred to the web version of this article.)

shoulder (1621 cm^{-1}), and a sharp and strong 2D peak (2700 cm^{-1}) (Fig. 9I-J), whereas OM6 is like OM5 but with a stronger D1-peak and D1/G up to 2, but without a significant 2D peak (Fig. 9K).

5. Discussion

5.1. Implications of the patterns and compositions in Doushantuo diagenetic spheroids

Chert concretions and apatite granules are commonly fossiliferous (Xiao et al., 2010; Muscente et al., 2015; She et al., 2014), which is a feature that suggests concretions are autochthonous in the original sediments (Seilacher, 2001). These objects also commonly contain circularly concentric layers and vary in size from 10^{-4} to 10^{0} m. Wave action cannot explain these characteristics, especially when the fossils are exceptionally preserved, and laminations are nearly perfect equidistant geometric patterns. Also, sedimentary reworking of detrital particles through wave action is admittedly a popular explanation for the origin of granules and rosettes, however there is no reason why this process should lead to radially aligned crystals, circular concentricity, twinned spheroids, cavity structures, and a limited range of dominant mineral composition. Biological processes and mechanical erosion by waves may still superficially influence some diagenetic spheroids, however COR well explains their most noteworthy features (Dodd et al., 2018). All the key features that describe the patterns in diagenetic spheroids and COR (Table 4) occur as circularly concentric and equidistant laminations, cavities, twins, concentration gradients, rounded asymmetry, and radial diffusion. Twinned microscopic dumbbells and layers are also known to form during the abiotic precipitation of proto-dolomite and apatite (Seilacher, 2001; Blake et al., 1998; Sánchez-Román et al., 2014), although they have also been suggested to form during biological activity associated with dolomitization (Liu et al., 2019). However, the new observations are clear: diagenetic spheroids exhibit the same kinds of self-similar patterns and have nearly the same range of magnitude of dimension sizes as those patterns produced in COR, hence they are more consistent with authigenic abiotic processes.

In addition to size and pattern similarities, both diagenetic spheroids and COR represent objects that share chemical similarities between substances of COR reactants and products (Table 4). Doushantuo diagenetic spheroids are composed of the typical substances found in fossils and dominated by quartz, apatite, carbonate, pyrite, and OM. Hence, the inferred precursor compositions of these phases include OM from biomass, carbonate anions, sulphate, and reduced iron, which is comparable to some of the reactants and products of COR that include carboxylic acids, CO_2 bubbles, sulphuric acid and sulphate, and ferrous iron in ferroin, respectively (Table 4). For iron, ferric phases have been reported in Cryogenian pyrite rosettes (Cui et al., 2018), although not in the Doushantuo diagenetic spheroids studied here. Strong oxidants such as iodate and bromate are used in COR and are known to have become more abundant in post-glacial Ediacaran seawater (Hardisty et al., 2014), including in the upper slope paleo-environment of the Doushantuo Fm (Wei et al., 2019). Iodide and bromide may be present in trace level in hydroxylated and halogenated minerals, and they occur in trace level in the studied samples (Table 2; Fig. 8A), presumably in apatite and phyllosilicates. Hence, halogen compounds were available during sedimentary diagenesis and could have become sufficiently concentrated in pore water solutions during dehydration to trigger COR. Therefore, higher concentrations of oxidized halogens and oxidants can then be coupled with biomass and redox-sensitive trace metals to produce COR patterns and their subsequent mineralization into diagenetic spheroids (Papineau et al., 2021; Varkouhi et al., 2022; Varkouhi and Papineau, 2023).

In the studied samples, the presence of key trace metals including Fe, Cr, Ni, Mn, Ti, V, Co, Mo, and Zn shows that these metals with variable oxidation states are also available catalysts during sedimentary diagenesis. This is relevant for COR because there are various redox-sensitive metals that can lead to self-catalysis of COR and to pattern formation (Belmonte et al., 1997). REEs also are found in the studied phosphorites with diagenetic spheroids and tend to be enriched therein, however such enrichments are not seen in the studied samples, when compared to Post Archean Australian Shales. In any case, sedimentary phosphorite does not always reliably preserve seawater REE compositions, which can be altered by diagenetic processes involving biomass decomposition (Shields and Webb, 2004). Here, the slightly positive Eu- and negative Ce-anomalies of some Doushantuo diagenetic spheroids are akin to those in older ferruginous chemical sedimentary rocks that also have various diagenetic spheroids such as banded iron formations of early Paleoproterozoic (Konhauser et al., 2018; Pecoits et al., 2009) and Eoarchean-Hadean age, although these have no Ce anomalies and more pronounced Eu anomalies (Papineau et al., 2022). Hence, the measured REE might indicate seawater composition despite the inferred diagenetic decomposition of biomass (see below). Some of these transition

Table 2
Trace elemental composition of selected specimens of diagenetic spheroids (all values in ppm).

		Congo Malachite	YG1801a *	YG1801b *	YG1803	D01706	ZK511–15	ZK511-32	ZK703–897.46	NBS120C§	NBS120C	
	Analytical method	Papineau (2020)	Botryoidal quartz, Member I	Botryoidal quartz, Member I	Chert concretion, Member II	Botryoidal quartz, Member I	Granular phosphorite Member II	Granular phosphorite, Member II	Concretionary botryoidal dolostone	Measured values	Certified values	Recovery %
Al	ICP-OES	401.50	1176.12	1199.17	1757.79	1073.49	5732.24	727.95	BDL	5508.48	5600.00	98.4
As	ICP-MS	33.28	1.04	0.90	52.10	6.65	14.43	14.42	1.02			
Ba	ICP-OES	39.81	2180.92	2271.14	208.14	270.41	159.25	235.90	1.86	59.60	61.00	97.7
Be	ICP-MS	11.27	0.10	0.11	0.17	0.17	3.62	0.55	0.02	2.33	2.86	81.6
Bi	ICP-MS	0.00	0.05	0.01	0.05	0.02	0.01	0.06	0.00			
Ca	ICP-OES	38.88	282,884	281,746	122,921	96,406	341,910	334,104	218,479	351,520	344,000	102.2
Cd	ICP-MS	0.00	0.27	0.28	0.12	0.10	BDL	1.06	BDL	21.51	18.00	119.5
Co	ICP-MS	199.47	2.86	2.69	6.17	5.21	4.64	2.73	1.25	3.85	2.85	134.9
Cr	ICP-MS	0.56	260.27	226.91	727.50	676.89	401.68	295.17	61.89	53.79	59.60	90.3
Cu	ICP-MS	552,697	BDL	BDL	15.26	BDL	BDL	BDL	BDL	7.78	8.60	90.4
Fe	ICP-OES	85.05	2590.56	2565.96	41,504.79	4209.31	7015.02	2473.60	530.27	7639.22	7700.00	99.2
K	ICP-OES	75.23	298.67	301.96	213.88	521.34	4933.50	BDL	49.04	1142.55	1000.00	114.3
Mg	ICP-OES	163.28	5273.98	5456.81	33,724.54	0.00	4127.62	24,437.28	128,854	1703.38	1700.00	100.2
Mn	ICP-MS	585.36	3122.44	3169.03	500.63	429.96	645.47	318.56	85.02	245.63	250.00	98.3
Mo	ICP-MS	0.14	2.27	2.26	9.96	7.53	4.10	BDL	1.90			
Na	ICP-OES	24.07	211.19	201.98	326.61	215.06	3028.95	2789.42	300.17	2222.36	2600.00	85.5
Ni	ICP-MS	17.97	97.15	91.98	352.19	261.51	156.44	123.80	24.15	13.47	17.00	79.2
P	ICP-OES	42,836.73	129.34	144.89	1825.43	170.73	140,386	121,859	299.91	184,952	150,700	122.7
Pb	ICP-MS	3.44	1.48	1.31	1.26	0.67	16.84	64.68	0.11			
Sr	ICP-MS		263.11	262.21	217.48	24.05	622.39	841.98	21.60	708.18	705.00	100.5
Ti	ICP-MS	6.91	43.35	41.29	321.69	52.16	242.71	11.30	2.24	887.52	900.00	98.6
V	ICP-MS	171.55	9.12	8.53	29.02	12.58	21.42	29.92	20.60			
Zn	ICP-MS	890.94	28.04	27.46	125.91	11.38	7.18	27.92	4.47	119.09	117.00	101.8
Sc	ICP-MS	1.91	0.04	0.17	0.34	0.20	0.81	0.06	0.00	6.69	6.40	104.5
Y	ICP-MS	6.66	1.82	1.92	5.36	0.87	56.64	12.90	0.22			
La	ICP-MS	0.37	0.98	1.04	10.25	0.41	19.03	3.72	0.05			
Ce	ICP-MS	0.34	1.66	1.36	9.56	0.78	35.03	4.73	0.08			
Pr	ICP-MS	0.14	0.21	0.22	1.97	0.12	5.30	1.04	0.02	18.24	17.40	104.8
Nd	ICP-MS	0.76	0.84	0.89	7.83	0.62	24.83	5.34	0.08	78.25	75.00	104.3
Sm	ICP-MS	0.36	0.18	0.20	1.39	0.22	5.62	1.33	0.02	15.99	23.00	69.5
Eu	ICP-MS	0.12	0.45	0.49	0.48	0.10	1.36	0.38	0.01	3.69	3.60	102.4
Gd	ICP-MS	0.73	0.22	0.23	1.36	0.21	6.90	1.73	0.02	18.68	18.90	98.8
Tb	ICP-MS	0.14	0.03	0.03	0.18	0.03	1.11	0.27	0.00	2.87	2.00	143.7
Dy	ICP-MS	0.89	0.20	0.21	0.93	0.17	7.18	1.64	0.02	17.82	17.20	103.6
Ho	ICP-MS	0.20	0.04	0.05	0.18	0.03	1.69	0.36	0.01	4.04	3.92	103.0
Er	ICP-MS	0.54	0.14	0.15	0.45	0.09	5.07	1.01	0.02	12.06	11.70	103.1
Tm	ICP-MS	0.07	0.02	0.02	0.06	0.01	0.70	0.13	0.00	1.68	1.10	152.3
Yb	ICP-MS	0.46	0.15	0.16	0.35	0.07	4.13	0.69	0.01	10.80	10.90	99.1
Lu	ICP-MS	0.07	0.03	0.03	0.05	0.01	0.59	0.10	0.00	1.73	1.70	101.8
Th	ICP-MS	0.31	0.12	0.14	0.40	0.23	0.66	0.10	0.19	7.00	8.00	87.4
Br	ICP-MS	80.91	BDL	BDL	0.99	2.06	0.88	4.35	7.55	1.04	0.69–0.99	105.3
I	ICP-MS	BDL	BDL	BDL	0.21	0.24	0.57	BDL	BDL	0.18	0.18–0.28	100.0
Cl	ICP-MS	BDL	BDL	BDL	128.33	219.33	243.82	1066.81	710.63	103.90	110–130	94.5
F	Ion Chromatography	BDL	BDL	BDL	315.87	BDL	25,855.85	16,982.18				

BDL stands for 'below detection limit'.

* a and b are different splits from the same sample to test analytical reproducibility and sample homogeneity.

§ NBS120C is a phosphorite geochemical standard.

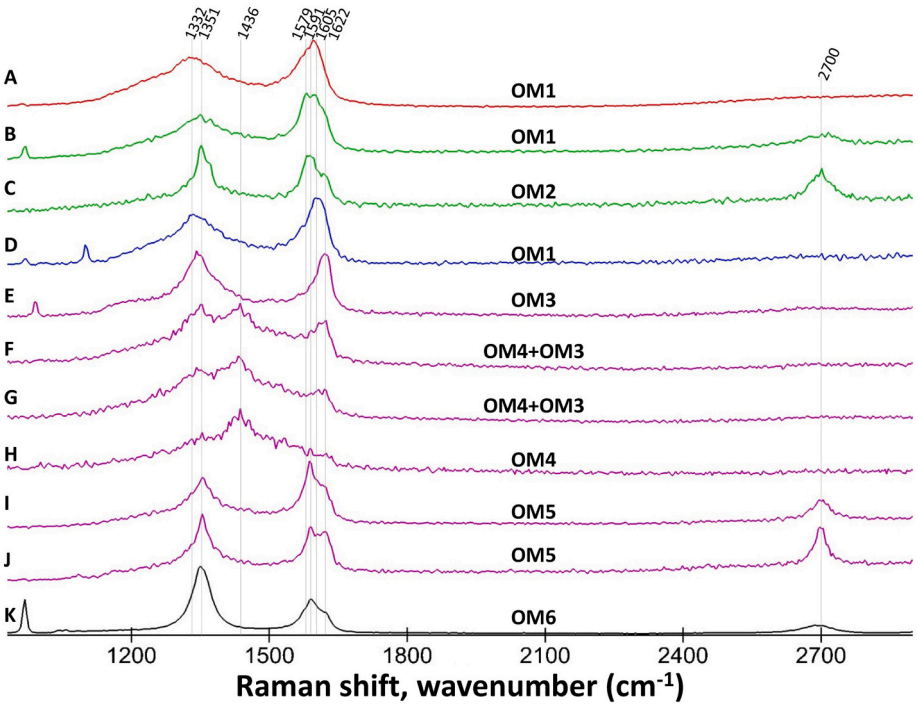

Fig. 9. Variably crystalline and functionalized organic matter from diagenetic spheroids in Doushantuo Formation. Raman spectra of various types of OM in granular phosphorite: (A) OM1 from *ZK115–33*, (B—C) OM1 and OM2 from *ZK511–15*, (D) OM1 from *ZK701–06*, and (E-J) OM3, OM4, and OM5 from *ZK115–12.* (K) OM6 is from concretionary phosphorite *13ZX1–6*.

metals and REE are redox-sensitive elements that can substitute for iron in ferroin to catalyse COR and produce patterns in experiments (Belmonte et al., 1997). While strong oxidants and acids as well as transition metals are common in both diagenetic spheroids and COR, more COR experiments are also needed to determine the range of reactants and their concentrations that can produce self-similar patterns. New proxies, perhaps based on bromine and iodine stable isotopes, might further constrain the range of concentrations of iodate and bromate in original diagenetic pore waters. In any case, diagenetic spheroids occur in a wide range of chemically precipitated and siliciclastic sedimentary rocks from throughout the geological record, and because the COR model is compatible with many different natural environments where the reactants occur, it is perhaps not surprising that the Doushantuo diagenetic spheroids contain a limited range of dominant minerals along with redox-sensitive trace elements.

5.2. The range of types of organic matter associated with Doushantuo diagenetic spheroids

In the Doushantuo Fm, OM1 is the dominant type within apatite granules and resembles OM types reported in different paleoenvironments of Doushantuo Members I and IV (Papineau et al., 2021; Wang et al., 2017; Cañadas et al., 2022; 2024). The variability noted for D1- and G-band positions, relative intensities, and full width at half maximum (Table 3) may be related possibly to variable levels of degradation, thermal metamorphic maturity, or imprint of primary versus secondary productivity. Besides, various mixtures with different proportions of types of OM may also occur and explain some of these variable relative intensities. Despite these considerations, we note two mineralogical connections between OM4 and pyrite-marcasite rosettes and pyrite framboids (Fig. 9G-I) and between platy OM2 and illite or sericite, identified by its 708 cm^{-1} and 3626 cm^{-1} peaks (Fig. 7F) (Table 3). First, OM2 is found in only one apatite granule laminated with botryoidal pyrite and it specifically occurs as a microscopic flake about 300 nm wide and 10 μm long (Fig. 7D-F), which is an unprecedented observation in a natural specimen, to our knowledge. This tiny object resembles graphene both in morphology and crystal structure, where its strong 2D peak has a similar relative intensity to the G-band and comparable to graphene (Elias et al., 2009), however it occurs as a stack of graphene sheets in Doushantuo. This is because OM2 has a platy habit within its host illite-sericite, and therefore OM2 is inconsistent with the habits of a graphite whisker (Tan et al., 2001) or of a carbon nanotube (Tan et al., 2002). Alternatively, an argument for graphene to be authigenic is that pure graphite does not occur in association with OM2, which would be expected to dominate the kinds of graphitic carbons in the rare rocks known to contain graphene. Other sources of OM from sedimentary detritus can thus possibly explain the occurrence of graphene OM2 outside of the apatite granule with pyrite botryoids (Fig. 7D-F). Other rocks have been reported to contain curled nanoscopic structures, tubes, cones, and whiskers with similar spectral features (Jaszczak et al., 2007). Turbostratic graphite, a form of disordered sp^2-carbon might also explain the Doushantuo graphene flake, which is thus consistent with several possible origins.

Second, OM4 in the pyrite-marcasite rosette has a prominent D5 peak at 1433 cm^{-1}, but also sharp D1- and G-peaks at 1355 and 1591 cm^{-1}. This unusual D5 peak could be due to sulphur functional groups in OM4. In fact, thiol groups in OM might explain the prominent 1433 cm^{-1} peak in OM4, associated specifically with pyrite-marcasite rosettes. Out-of-equilibrium mineral assemblages include barite [$BaSO_4$] inclusions inside pyrite-marcasite rosettes (Fig. 7H) (Jiao et al., 2023b), which can be considered as evidence for redox reactions involving sulphate, biomass, and iron. However, other functional groups may also be possible for the 1433 cm^{-1} peak possibly linked to the co-occurrence of diamondoids, which are common in crude oil (Chen et al., 1996; Dahl et al., 1999) and have sharp Raman peaks located at similar wavenumber positions (Filik, 2006). While a more specific determination of the substances in OM2 and OM4 awaits further analysis, OM1 to OM6 can be broadly interpreted as indicative of variable mixtures of disordered to crystalline forms of sp^2 and sp^3 bonded carbon atoms, consistent with thermal cracking of biomolecules.

Observations also show diagenetic spheroids are ubiquitously associated with OM and commonly associated with fossils. This

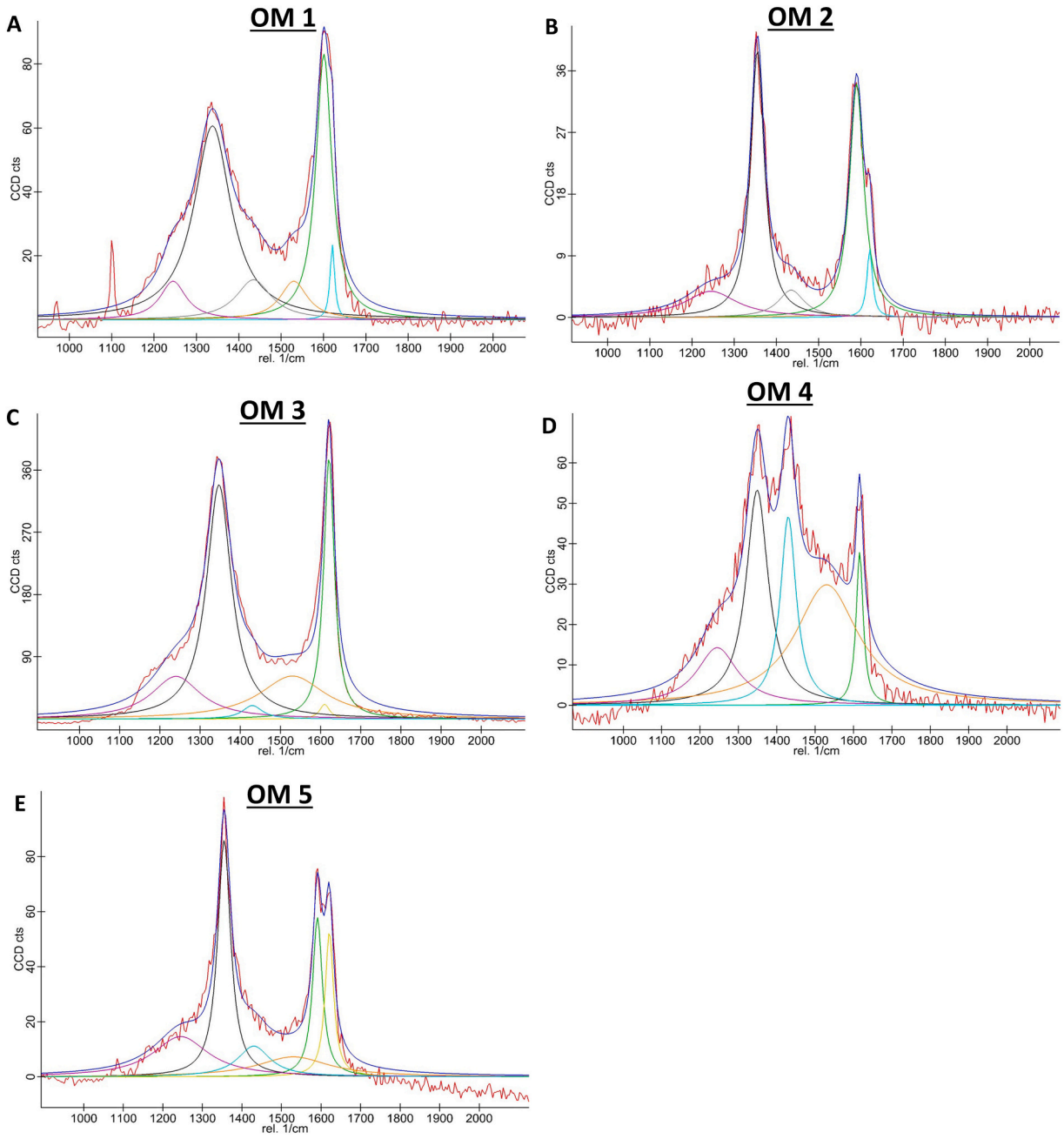

Fig. 10. Comparison of the six types of organic matter reported in Member II of the Doushantuo Formation. (A) Raman spectrum of OM1 (*ZK701–6*), (B) Raman spectrum of OM 2 (*ZK511–15*), (C-E) Raman spectra for OM3, OM4, and OM5 (*ZK115–12*).

demonstrates that the source of OM for the inferred COR in the original sediments was biomass. Hence, the origin of the various types of OM associated with fossils and diagenetic spheroids may be multi-fold and could also include OM from variably differentiated organisms implying heterogeneous biochemical compositions, or from biomass variably affected by COR and low thermal metamorphism, which can affect levels of preserved molecular functional groups. Raman spectra of OM in Doushantuo diagenetic spheroids are varied and cannot all be explained by variable metamorphic imprints. A later source of OM remobilised from other rocks is inconsistent with petrographic evidence of finely disseminated OM1 and OM5 (Fig. 7) in nanoscopic apatite and quartz, and with the absence of veins with remobilised OM. We caution however that these observations show an unusual occurrence of OM2 associated with diagenetic spheroids, hence an older source of OM cannot be discounted form some Doushantuo OM. Similar observations for OM4 and OM5 in pyrite-marcasite rosettes and pyrite framboids expand the range of known OM types associated with diagenetic spheroids in such low-grade metamorphic rocks. Variable OM types are generally consistent with an authigenic origin and thus support the COR model for the involvement of biomass in the origin of diagenetic spheroids in the Doushantuo Fm.

5.3. *Discussion of abiotic carbon cycling in the Doushantuo Formation*

The stratigraphic and paleo-geographic distribution of diagenetic spheroids show that the concentration of chert nodules, carbonate concretions, and lenticular beds is highest in the shallow shelf and upper slope paleo-environments and throughout all four Doushantuo members (Zhu et al., 2013; Muscente et al., 2015). This correlation of diagenetic spheroids and paleo-environments is also related to multiple negative

Table 3
Comparison of patterns and substances through Raman spectral features of organic matter occurrences in Doushantuo member II diagenetic spheroids (see modelled spectra in Fig. 10).

Raman Peaks	Parameter	OM1	OM2	OM3	OM4	OM5
	Mineral association Diagenetic spheroids	apatite + pyrite botryoids, granules, rosettes	apatite + illite granules with botryoid	apatite + pyrite botryoids, granules, rosettes	pyrite + marcasite + apatite + quartz + barite rosettes	pyrite + marcasite + apatite + quartz + barite rosettes
G	**Position**	1601	1590	1622	–	1591
	FWHM	46	41	30	–	30
	Area	6005	2200	1000	–	2730
D1	**Position**	1338	1355	1347	1349	1355
	FWHM	106	40	75	70	40
	Area	10,080	2450	39,335	5859	2730
D2	**Position**	1621	1621	1621	1616	1621
	FWHM	13	16	32	22	26
	Area	480	250	19,000	1310	2150
D3	**Position**	1530	1530	1530	1530	1530
	FWHM	78	180	200	200	220
	Area	1485	100	19,500	9362	2500
D4	**Position**	1245	1245	1240	1245	1245
	FWHM	75	150	150	130	170
	Area	1417	900	14,500	2908	3900
D5	**Position**	1435	1435	1430	1435	1430
	FWHM	100	75	60	130	100
	Area	1970	470	1832	2908	1750
2D	**Position**	ca. 2700	2701	ca. 2700	2700	2700
	FWHM	300	55	220	29	29
	Area	4560	1670	19,000	2863	2858
Correlation	**(R)**	0.9878	0.9843	0.9891	0.9813	0.9851
Peak T_{Lafhid}	**RA1**	**248**	**296**			**229**
Peak T_{Lafhid}	**RA2**	**261**	**232**			**140**

excursions of C isotopes in carbonates (Zhu et al., 2013; Lan et al., 2018), highly variable seawater sulphate (McFadden et al., 2008; Li et al., 2010), and with higher iodine abundance (Wei et al., 2019) (Fig. 2G). In nature, the highly soluble elements bromine and iodine can be concentrated in algae and be involved in a wide range of bacterial metabolisms (Leri et al., 2010). While it is unknown whether there is halogenated OM in the Doushantuo Fm, the inferred co-occurrence of iodate and sulphate supports the new model of COR (Fig. 11) to explain the formation of diagenetic spheroids from the abiotic decarboxylation of biomass. This explanation can then possibly be related to the multiple negative carbon isotope excursions in the Doushantuo Fm and future analyses will show a broader applicability of the COR model to diagenetic spheroids from throughout Earth history.

In Member I of the Doushantuo, there is evidence for varying levels of seawater sulphate as recorded by fluctuating levels of carbonate-associated sulphate and ^{34}S-enrichments around +25 ‰, and up to +40 ‰, and occurring in ^{13}C-depleted carbonate (Huang et al., 2013) (Fig. 2D, F). Sulphide rosettes in the Cryogenian Datangpo Fm have extreme ^{34}S enrichments up to +70 ‰, they have 'petals' of pyrite or iron oxide, and they are associated with botryoidal rhodochrosite [$MnCO_3$], which have been interpreted as abiotic reaction products (Cui et al., 2018). Such microscopic rosettes display circular concentricity and radially aligned crystals and they have a similar range of minerals as granules, concretions, and botryoids, all of which are also dominated by quartz, apatite, pyrite, or carbonate (Cui et al., 2018). The nanoscopic size of marcasite and OM in quartz rosettes suggests limited alteration by metamorphism and a diagenetic origin consistent with the oxidation of biomass by sulphate. Biological sulphate reduction and sulphide oxidation can lead to strong sulphur isotope fractionations in the Doushantuo Fm where authigenic pyrite grains have a large range of $\delta^{34}S$ values consistent with various microbial metabolic pathways and fluctuations in seawater and pore water sulphate concentration (McFadden et al., 2008; Cui et al., 2018). Highly variable sulphur isotope ratios after the Marinoan glaciation in South Australia concurs with the interpretation of variable seawater sulphate and microbial fractionation (Halverson and Hurtgen, 2007). Contemporary acidic conditions also likely existed because sulphate is believed to originate from oxidative weathering of older crustal pyritiferous exposures that can lead to conditions like acid-mine-drainage (Konhauser et al., 2011). Such sources of sulphate and protons represent key reactants for abiotic spontaneous COR proposed to take place during the diagenetic decomposition of biomass in chemical sediments. Hence, there are some significant stratigraphic fluctuations in post-glacial seawater sulphate, and they are associated with negative carbon isotope excursions in Doushantuo carbonates. These signals demonstrate the availability of sulphate, which could also have contributed to the abiotic decomposition of biomass, and is consistent with the presence of diagenetic sulphate and sulphide minerals in rosettes, granules, botryoids, and concretions. Hence, we argue the decomposition of biomass was abiotic (Cui et al., 2018), although microbial sulphate reduction and sulphur oxidation could plausibly have played a role as well (McFadden et al., 2008; Li et al., 2010; Cui et al., 2018).

Lastly, the compound ferroin is used in COR to create contrasting colours and gradients of colours of the characteristic patterns. The analogue of this N-bonded Fe complex in diagenetic pore water solutions could be similar macromolecular cofactors (i.e. tetrapyrroles) from decayed macromolecules from cellular electron transport chains in decayed membranes, such as heme or cytochromes, which also have a centralised, redox-sensitive Fe atom bonded to several N in polycyclic macromolecules (Papineau et al., 2023). In some cases, however, iron could simply become concentrated in pore water as an oxide or hydroxide and directly participate in chemical reactions. No matter the exact process, there certainly was Fe in the pore waters of many studied samples because pyrite and marcasite are commonly associated with Doushantuo diagenetic spheroids (Figs. 5–7). These minerals occur as circularly concentric rosettes, rims of granules, circularly concentric layers in concretions, and in rosettes, which is akin to the sulphide expected to be produced during abiotic sulphate reduction of ferric iron, but not of OM. It is also possible that Ti^{4+} might play a catalytic role associated with biomass oxidation because nanoscopic TiO_2 polymorphs are common in Doushantuo diagenetic spheroids, and they are known to abiotically catalyse the adsorption and oxidation of functionalised

Table 4
Features of COR and diagenetic spheroids with comparisons of their patterns and substances.

Objects / Compared features	Chemically oscillating reactions in Petri dish	Doushantuo diagenetic spheroids
Patterns		
Circularly concentric and equidistant laminations	Fig. 3A-C, 5Q-U	Fig. 3E-H, 5A-P, 6A-D, 7G-H
Circularly concentric equidistant laminations spanning several orders of magnitude in dimension size	Fig. 3A-C, 5Q-U	Fig. 3D-K, 5A-P, 6A-L
Cavity-shaped structures	Fig. 5Q-S	Fig. 3D-E, 5A, 5F-J, 6E-L
Twinned chemical waves (destructive interference)	Fig. 3C, 5Q-S	Fig. 3D, E, 5A, C, F-H, 5J, 5O, 6E-L
Rounded asymmetric concentric laminations	Fig. 3A	Fig. 3F-K, 5A, 5G, 5I
Radial diffusion or geometry	Fig. 3A-C, 5Q-U	Fig. 3B, 5G, M, O, 7G-H
Colour gradients in laminations	Fig. 5Q-U	Fig. 3F, 5A-B, 5H, 5K, 6B, 6J
Substances		
Organic reactants (electron donors)	Malonic acid, carboxylic acids	Carboxylic acids[1] (always present in biomass), now as residual OM1 to OM6 and organic microfossils (Fig. 6M-Q)
Strong oxidants - halogens	Iodate, bromate, perchlorate	Iodate and bromate[2] (in apatite and carbonate)
Strong acids - sulphur	Sulphuric acid, sulphate	Sulphate (in barite)
Redox-sensitive metals	Ferroin, Ce, Mn	Fe (in pyrite and marcasite)
Product carbonate	CO_2 bubbles	^{13}C-depleted carbonate minerals (in diagenetic calcite and dolomite)

[1] See Papineau et al. (2021) and (2016) for carboxyl functional groups in Cambrian and Paleoproterozoic sedimentary organic matter, respectively.
[2] See Wei et al. (2019) and Hardisty et al. (2014) for iodate concentration in Precambrian carbonates. Bromate behaves like iodine, but it is seldom measured in Precambrian apatite and carbonate.

organic acids (Cleaves et al., 2010; Fujishima and Zhang, 2006). Hence, redox-sensitive transition metals were present in Doushantuo diagenetic environments, and they likely participated as catalysts involved in abiotic carbon cycling and the formation of diagenetic spheroids.

5.4. On the formation of diagenetic spheroids in the geological record

As the origin of most diagenetic spheroids is still uncertain and a subject of debate, the new observations and COR model presented in this work are timely, yet complex, because a comprehensive link requires multiple and distantly related scientific disciplines. The following subsections are organised primarily by the types of diagenetic spheroids to describe advances that the COR model provides over other previously invoked formation models.

5.4.1. The unclear origin of concretions and nodules

Field observations give important information on the origin of concretions and nodules as bedding laminations can commonly be followed into many of these objects, which shows that concretions formed after sedimentation and specifically after compaction when they do not deflect sedimentary laminations, or during early diagenesis when sedimentary laminations are warped around them (Marshall and Pirrie, 2013). Concretions and nodules also commonly contain organic-rich or pyritised fossils or borrows, usually located near their geometric centre, which has led to the interpretation that nucleation occurred around decayed visceral tissue or faecal matter in the presence of diagenetic solutions rich in sulphur and iron (Wilson and Brett, 2013; Bernard et al., 2010; Seilacher, 2001). Localised anoxic and alkaline conditions in sediment pore waters during diagenesis are usually regarded as necessary for the formation of carbonate concretions (Berner, 1968). Stable isotopic composition of carbon and sulphur in concretions and nodules have been used to trace various microbial metabolisms associated with biomass decomposition such as fermentation and sulphate reduction (Irwin et al., 1977; Xiao et al., 2010; Plet et al., 2016), and even methanogenesis in some cases (Cotroneo et al., 2016). Within carbonate concretions there are also commonly ferruginous carbonate and sulphide minerals as well as OM, which can contain various molecular functional groups, thereby indicating a biological source of carbon in carbonate and the preservation of organic biomarker molecules (Bernard et al., 2010; Plet et al., 2016).

Concretions and nodules in the geological record are dominantly composed of carbonate, apatite, chert, and/or sulphide and these phases are usually associated with OM. Many models proposed for the formation of concretions involve microorganisms and/or secondary nucleation associated with groundwater during diagenesis. The growth of concretions and nodules is sometimes interpreted to involve the microbially-mediated decomposition of biomass during diagenesis; however, this does not explain mineral patterns with circular concentricity and radial geometries. For these patterns, other previous models include concentric growth from the core nucleus with successive layer added onto the core (Oertel and Curtis, 1972), or the development of sphericity in concretions occurring as the inward diffusion from an initially precipitated outer shell followed by inner core formation (Coleman, 1993; Coleman and Raiswell, 1995). The layered circular concentricity in diagenetic concretions from the Doushantuo Fm has been suggested to follow a paragenetic sequence that involved early diagenetic phosphatisation, pyritization during early and late diagenesis and the formation of diagenetic carbonate during early compaction until late diagenesis (Schwid et al., 2021). While the latter proposed paragenesis was used to argue that discoidal features in rocks are probably pseudofossils rather diagenetic features, OM is ubiquitous in all specimens and thus it is likely involved in the proposed abiotic reactions as argued above. Another relevant comparison may be with glendonites, which are radiating carbonate structures, presumed pseudomorph of ikaite [$CaCO_3 \bullet 6H_2O$] and associated with cold-water settings (Rogov et al., 2021). Carbonate and silicified glendonites are associated with OM and concretions in the Doushantuo Fm (Wang et al., 2017; Wang et al., 2020) and therefore, their radiating morphology and other geometric characteristics should be investigated in the context of COR in future research. Hence, considering the new COR model, a similar

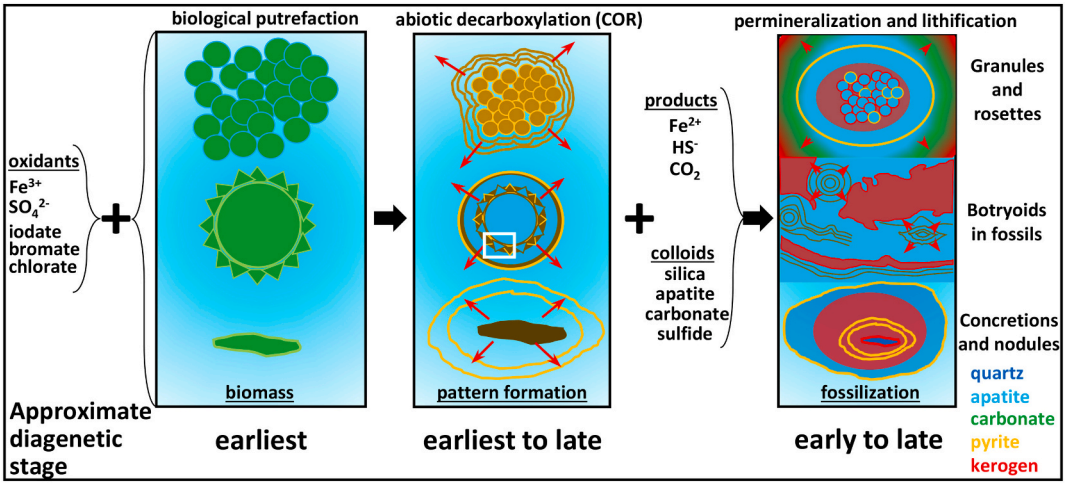

Fig. 11. Model of COR and other reactions to explain the mineralogy and patterns of diagenetic spheroids in the Doushantuo Formation. The model illustrates the growth of granules or rosettes around microorganisms or biomass (top), botryoids inside acritarch fossils (middle), and concentric layers in concretions and nodules (bottom). Botryoids inside acritarch fossils are shown as an inset (white rectangle). Red arrows represent the interpreted direction of radial diffusion of chemical waves with lists of relevant possible oxidants, reaction products, and nanoscopic colloids. Approximate diagenetic stages are interpreted in the bottommost row with earliest diagenesis taking place in the water column and/or at the sediment-water interface, early diagenesis taking place after deposition until shortly after burial, and late diagenesis during dehydration reactions and permineralization, until lithification. (For interpretation of the references to colour in this figure legend, the reader is referred to the web version of this article.)

sequence of mineralization is proposed here as an alternative explanation (Fig. 11), with the main distinction that only the COR model predicts the formation of specific patterns and compositions observed in concretions and nodules as well as a specific role for OM to fuel the abiotic reactions.

5.4.2. *The debated origin of granules*

The most common formation model proposed for granules is through wave-action or sedimentary re-working that causes detrital particles or precipitates to become rounded on sedimentary hardgrounds (Simonson, 1985; Pufahl and Grimm, 2003). Although this is not easily reconcilable with the fact that granules commonly occur in chemically precipitated sedimentary rocks – chert, jasper, and phosphorite –, granules have also been considered a post-depositional diagenetic replacement texture (Hiatt et al., 2015; Papineau et al., 2017). In chemical sedimentary rocks, mineral precipitation in granules could occur through flocculation or aggregation in the water column, or at the sediment-water interface (Simonson, 1985; She et al., 2013; Stefurak et al., 2015). Direct microbial activity for the rounding of granules might also explain some of their characteristics (Dahanayake and Krumbein, 1986), however it is only recently that the COR model has been suggested to explain the abiotic formation of geometric patterns in chert granules during diagenesis (Papineau et al., 2017; Dodd et al., 2018). Alternatively, apatite granules commonly display concentric layers of minerals, sometimes including pyrite laminations, which is indicative of formation during early diagenesis and from the influence of iron, sulphate, and OM (Pufahl and Grimm, 2003; Papineau et al., 2017; Dodd et al., 2018). Diagenetic formation models for Phanerozoic apatite granules are usually based on a combination of processes involving redox-aggradation, unconformity-bound rounding, and biomass decomposition (Pufahl and Grimm, 2003). Early diagenetic processes in granules are consistent with 1) their common content of relatively well-preserved microfossils (Lougheed, 1983; Walter et al., 1976; Schopf and Kudryavtsev, 2012; She et al., 2014; Papineau et al., 2017; Dodd et al., 2018), 2) their micro-textural evidence indicative of a pre-compaction timing of formation (Maliva et al., 2005), as well as 3) their common association with stromatolites or other fossils, OM, ^{13}C-depleted carbonate, and authigenic apatite [$Ca_5(PO_4)_3(OH,F,Cl)$] (Pufahl and Grimm, 2003; Papineau et al., 2017; Dodd et al., 2018). Hence, granules have an uncertain origin, possibly involving wave-action, microbial activity, and post-depositional early diagenetic processes.

New observations of apatite granules with later diagenetic coatings of isopachous apatite also form cavity structures between tightly packed granules (Figs. 5, 6; Simonson, 1985), which is further consistent with a pre-compaction timing during early diagenesis. It is possible that these processes begin in water column or at the sediment-water interface (She et al., 2013). Furthermore, the COR model implies redox reactions to also be involved, which lends support also to the redox aggradation model (Pufahl and Grimm, 2003) but goes further and suggests a specific role for biomass decomposition in the growth of granules (Papineau et al., 2017; Dodd et al., 2018). This specifically predicts and explains the formation of circularly concentric features through diffusion, which are fuelled by the abiotic decarboxylation of OM. In natural environments on Earth, OM almost exclusively comes from biomass. The diffusion process in the COR model thus elegantly explains the occurrence of microfossils, as the source of carboxylic acids, inside granules of apatite (Fig. 11) (She et al., 2013, 2014), granules of quartz (Walter et al., 1976; Schopf and Kudryavtsev, 2012; Gabriel et al., 2021), and granules with hematite and magnetite (Lougheed, 1983; Dodd et al., 2018). However, it is also conceivable that on a lifeless planet, abiotic granules could form from abiotically synthesized and abiotically decarboxylated OM. Hence, the COR model does not invalidate previous models, but it is the only model that explains the patterns inside granules, their mineral composition rich in carbon, phosphorous, sulphur, and iron (which has variable oxidation states), as well as their common content of microfossils.

5.4.3. *The enigmatic formation of rosettes and pyrite framboids*

Various types of microscopic rosettes with circular concentricity are composed of radially aligned apatite, quartz [SiO_2], and carbonate and these ubiquitously occur with OM in stromatolitic phosphorite (Papineau et al., 2016), in cherty black shale (Mossman et al., 2005 – called "spherules" therein), and in granular chert and jasper from the late Paleoproterozoic (Lougheed, 1983; Heaney and Veblen, 1991; called "spherulites" in both). Rosettes composed of stilpnomelane [$K(Fe^{2+},Mg,Fe^{3+})_8(Si,Al)_{12}(O,OH)_{27}\bullet n(H_2O)$] or hematite [$Fe_2O_3$] and chert also occur in banded iron formations and commonly with carbonate (Grenne and Slack, 2003 – called "spherules" therein; Rassmusen et al., 2013 – called "microgranules" therein; Dodd et al., 2018; Papineau et al., 2022), including in association with Earth's oldest purported

microfossils (Dodd et al., 2017; Papineau et al., 2022). An early diagenetic origin of rosettes seems consistent with their occasional preservation inside nodules (Rassmusen et al., 2013) and inside or beside granules (Dodd et al., 2018). A direct role for OM in natural pyrite framboid formation has long been suspected given that diagenetic experiments using biomass produce radially aligned, circularly concentric, and twinned microscopic spheroids of iron phosphate associated with nanoscopic sized (i.e. 200 nm to 1 μm in diameter) pyrite spherules, considered as precursors of pyrite framboids (Duverger et al., 2021; Truong et al., 2023). In fact, carbon to nitrogen ratios of OM inside natural pyrite framboids suggest that biomass is likely an important reactant for their formation (Wacey et al., 2014). Framboidal pyrite is commonly associated with large sulphur isotope fractionations that suggest microbial sulphate reduction as a dominant process, and therefore point to diagenetic and metabolic reactions involving sulphate, iron, and OM in environments with variable redox conditions (Gorjan et al., 2007). The variable diameter of pyrite framboids has also been used to trace the redox conditions of sedimentary environments (Wilkin et al., 1996), including during the Jurassic (Wignall and Newton, 1998), Permian-Triassic (Gorjan et al., 2007) and Ediacaran periods (She et al., 2016; Jiao et al., 2023a).

Sedimentary pyrite forms during early to late diagenesis and it can occur as framboids that can be twinned when closely packed, or it can form circularly concentric marcasite rosettes in chert, pyrite-marcasite rosettes, and concentric layers and rims inside granules and concretions (Figs. 3 and 5). In all these Fe-sulphide-bearing objects, different kinds of OM have a crystallinity and disorder consistent with the metamorphic grade of the host rocks, all with maximum peak temperature less than 300 °C (Table 3). The studied rosettes, including pyrite framboids and pyrite-marcasite rosettes, are systematically associated with different types of OM and specific geometric patterns, which is comparable to observations from diagenetic experiments (Köhler et al., 2013; Duverger et al., 2021). It is argued that pyrite framboids and pyrite-marcasite rosettes in the Doushantuo specimens studied in this work form abiotically, in agreement with previous experimental inferences (Ohfuji and Rickard, 2005). The different types of OM, all exposed to similar peak metamorphic temperatures, thus suggests variable processing and molecular functional group composition, as well as variable redox reactions during diagenesis, or in other words, out-of-equilibrium conditions. Carbonate and apatite rosettes are also systematically associated with OM and can display spheroidal twinning, circular concentricity, and radial patterns (Figs. 5 and 6). Hence, while it is commonly accepted that microscopic rosettes have a diagenetic origin, and they have been considered as dubiofossils (Heaney and Veblen, 1991; Chauhan, 1979), the COR model provides a more comprehensive explanation and a specific model for their abiotic formation in nature. This is because the COR model is consistent with the limited range of dominant minerals in rosettes (i.e. minerals rich in carbon, phosphorous, iron, sulphur, and silicon, which is like those of granules and concretions), and predicts the specific patterns they contain. Hence, the abiotic COR model does not disprove previous models, but more elegantly explains the patterns and mineralogy of rosettes, as well as their common association with OM, fossils, and other types of diagenetic spheroids.

5.4.4. *Advances on the origin of botryoidal mineral habits*

Botryoidal malachite displays repeating circularly concentric gradients of green shades and they can contain phosphorous enrichments, laminations with microscopic rosettes, and OM shaped as stromatolites and *Frutexites* in their geometric centres (Papineau, 2020). Botryoidal quartz habits in chert display circularly concentric and radial geometries that have lamination with concentration gradients composed of OM, geometric centres enriched in OM, and associations with disseminations of micron-size calcite, hematite, or pyrite (Papineau et al., 2021; Varkouhi et al., 2022; Varkouhi and Papineau, 2023; Papineau, 2024). In cherty dolomitic microdigitate stromatolites, there can be botryoidal chert layers with mineral mixtures of ferric-ferrous oxides and OM located specifically in the geometric centre of botryoids (Goodwin and Papineau, 2022) or associated with microfossils composed of OM (Gabriel et al., 2021; Yang et al., 2022). Botryoidal habits of quartz and apatite co-occur in association with cavities (Fig. 3D-E; Papineau et al., 2021), with rosettes (Fig. 5B), inside granules (Fig. 5C-D), and inside microfossils (Fig. 5E-F), which expands known observations for botryoid occurrences and the Doushantuo Fm. In the studied rocks, the minerals that compose botryoids are dominated by quartz and apatite, whereas accessory phases include carbonate, pyrite, and OM. Occurrences of microscopic botryoidal laminations of pyrite and OM inside apatite granules and inside microfossils show the same kinds of self-similar patterns and compositions as those in concretionary cavities, which demonstrates that these botryoids probably form during diagenetic COR from the decomposition of carboxylic acids in biomass, prior to their permineralisation in silica and apatite (Fig. 11). Their self-similar patterns occur over five orders of size dimension, from tens of micrometres to decimetres, which is consistent with the interpretation that botryoidal mineral habits represent fractal patterns: they are like each other over all size scales for these objects (Papineau, 2020, 2024; Papineau et al., 2021, 2023).

6. Conclusions and advances in understanding the origin of concretionary objects

Fractal patterns are geometric objects and shapes that appear self-similar at various size dimension scales. Compared to previous works, the most significant advance in this work is that the common association of rosettes inside botryoids, botryoids inside granules, and the multitude of comparable self-similar patterns and compositions between granules, concretions, and nodules further points to all these objects forming a continuum of diagenetic spheroids. Diagenetic spheroids can thus be interpreted as fractal objects because they are self-similar over all sizes in which they occur. This novel perspective is central to the COR model of formation, whereby geometric patterns form naturally and spontaneously during the diagenetic decarboxylation of carboxylic acids from biomass. In sedimentary systems, reaction products and residual reactants of COR ultimately mineralise as spheroidal carbonate, OM, quartz, apatite, pyrite, barite, and iron oxides. In the Doushantuo Fm, the source of OM associated with botryoids is decomposed biomass, as can be argued from the common occurrence of microfossils (Xiao et al., 1998, 2014; She et al., 2013, 2014). Ultimately, botryoids, concretions, nodules, granules, and rosettes can all conceivably be completely abiotic in origin, as their abiotic formation through COR could also be fuelled by abiotically synthesized carboxylic acids. In the Doushantuo Fm however, the collective evidence rather points to a biological source of carboxylic acids, processed abiotically during diagenesis.

Patterns in COR are closely similar to those in diagenetic spheroids from the Doushantuo rock record (Table 4). These patterns include circular concentricity, equidistant laminations, orders of magnitude of dimension sizes, cavity structures, colour or compositional gradients, spheroidal twins, rounded asymmetric laminations, and radial diffusion or geometry. In this new light, the radially expanding chemical waves of COR are comparable to the radial alignment of elongated crystals in diagenetic spheroids and can be used to predict the propagation direction of circularly concentric laminations during diagenesis (Fig. 11). This new COR model in nature is centered on the abiotic decomposition of dead organisms, which fuels these reactions to produce self-similar patterns inside diagenetic spheroids. These reactions require specific substances that include carboxylic acids, strong oxidants, strong acids, and redox-sensitive metals, which are comparable between diagenetic spheroids and COR (Table 4). The COR model thus explains some of the defining geometric features of diagenetic spheroids and why they have a limited range of mineralogy. In this light, the microfossils contained in granules, including the oldest purported fossil animal embryos (Xiao et al., 1998), are akin to macroscopic fossils inside concretions and the

biomass of the organisms is interpreted to have provided the fuel (i.e. carboxylic acids) for COR to spontaneously take place. Hence, the comparison between liquid-state and dynamic COR and solid-state diagenetic spheroids is solidly supported by several specific and defining patterns, and also supported by considerations of specific similarities in chemical compositions.

The new COR model provides an elegant explanation for the origin of circularly concentric patterns in concretions, nodules, granules, botryoids, and rosettes, which have all been considered as partly enigmatic and widespread in the Doushantuo Fm and beyond. These reactions also provide a new basis to understand the three negative $\delta^{13}C_{carb}$ excursions EN1-EN3 in the Doushantuo Fm as possibly authigenic and diagenetic in origin. During the deglaciation of snowball Earth and its aftermath, COR were likely stimulated by favourable environmental redox conditions and increased reactants, concentrated by both biological and diagenetic processes. Building on previous works, the COR model described here provides a significant geochemical advance to understand the mineralogy and significance of many more types of diagenetic spheroids, unifying these types under the umbrella of abiotic carbon cycling, which has implications for taphonomic processes associated with fossilisation and global biogeochemical cycles. Hence, the striking similarities between the self-similar patterns and substances of diagenetic spheroids and COR predicts that these objects are sedimentary-geochemical proxies for abiotic decarboxylation reactions in the sedimentary carbon cycle on Earth as well as on other planetary bodies.

CRediT authorship contribution statement

Dominic Papineau: Writing – original draft, Visualization, Validation, Supervision, Resources, Project administration, Methodology, Investigation, Formal analysis, Data curation, Conceptualization. **Zhenbing She:** Writing – review & editing, Visualization, Supervision, Resources, Investigation, Funding acquisition, Formal analysis. **Liangxuan Jiao:** Visualization, Methodology, Investigation. **Shuzhan Liu:** Visualization, Methodology, Investigation. **Deng Liu:** Writing – review & editing, Resources, Investigation, Funding acquisition. **Genming Luo:** Writing – review & editing, Investigation. **Chao Li:** Writing – review & editing, Investigation.

Funding

This work was supported by the National Key Research and Development Program of China (2023YFC2906601) and National Natural Science Foundation of China (grant # 42172337, 42130208 and 42272046).

Declaration of competing interest

The authors declare no competing interests that could appear to influence the work reported in this paper.

Acknowledgements

DP and ZS thank Q. Chen and C. Deng for their help in field work. G. Tarbuck is thanked for help with geochemical analyses in bulk powders. DP and ZS also acknowledge support from the Bureau of Geology and Mineral Resources of Guizhou Province for access to their core library. DP acknowledges J. Davy for fabricating some of the polished petrographic thin sections studied.

Data availability

All data is available in the manuscript"

References

Ader, M., Macouin, M., Trindade, R.I.F., Hadrien, M.-H., Yang, Z., Sun, Z., Besse, J., 2009. A multilayered water column in the Ediacaran Yangtze platform? Insights from carbonate and organic matter paired $\delta^{13}C$. Earth Planet. Sci. Lett. 288, 213–227. https://doi.org/10.1016/j.epsl.2009.09.024.

Algabri, M., She, Z., Jiao, L., Wang, G., Papineau, D., Zhang, C., Tang, D., Ouyang, G., Zhang, Y., Chen, Q., Li, C., 2020. Glaucony-phosphate association in the Ediacaran Doushantuo Formation, South China and its implications for marine redox conditions. Precambrian Res. 347, 105842. https://doi.org/10.1016/j.precamres.2020.105842.

Barfod, G.H., Albarède, F., Knoll, A.H., Xiao, S.H., Télouk, P., Frei, R., Baker, J., 2002. New Lu- Hf and Pb-Pb age constraints on the earliest fossils. J. Paleontol. 74, 767–788.

Belmonte, A., Ouyang, Q., Flesselles, J.-M., 1997. Experimental survey of spiral dynamics in the Belousov-Zhabotinsky reaction. J. Phys. II EDP Sciences 7, 1425–1468.

Belousov, B.P., 1958. A periodic reaction and its mechanism. In: "Sbornik Referatov po Radiatsionni Meditsine" (Megdiz, Moscow), p. 145 [in Russian].

Bernard, S., Benzerara, K., Beyssac, O., Brown Jr., G.E., 2010. Multiscale characterization of pyritized plant tissues in blueschist facies metamorphic rocks. Geochim. Cosmochim. Acta 74, 5054–5068.

Berner, R.A., 1968. Calcium carbonate concretions formed by the decomposition of organic matter. Science 159, 195–197. https://doi.org/10.1126/science.159.3811.195.

Blake, R.E., O'Neil, J.R., Gracia, G.A., 1998. Effects of microbial activity on the $\delta^{18}O$ of dissolved inorganic phosphate and textural features of synthetic apatites. Am. Minerol. 83, 1516–1531.

Bristow, T., Bonifacie, M., Derkowski, A., Eiler, J.M., Grotzinger, J.P., 2011. A hydrotherrmal origin for isotopically anomalous cap dolostone cements from South China. Nature 474, 68–71. https://doi.org/10.1038/nature10096.

Cañadas, F., Papineau, D., Leng, M.J., Li, C., 2022. Extensive primary productivity promoted the recovery of the Shuram excursion. Nat. Commun. 1-9. https://doi.org/10.1038/s41467-021-27812.

Cañadas, F., Papineau, D., She, Z., 2024. Biotic and abiotic processes in Ediacaran spheroid formation. Front. Earth Sci. - Earth and Planet. Mat. 1405220. https://doi.org/10.3389/feart.2024.1405220.

Chan, M.A., et al., 2019. Deciphering biosignatures in planetary contexts. Astrobiology 19, 1–28. https://doi.org/10.1089/ast.2018.1903.

Chauhan, D.S., 1979. Phosphate-bearing stromatolites of the Precambrian Aravalli phosphorite deposits of the Udaipur region, their environmental significance and genesis of phosphorite. Precambrian Res. 8, 95–126.

Chen, J., Fu, J., Sheng, G., Liu, D., Zhang, J., 1996. Diamondoid hydrocarbon ratios: novel maturity indices for highly mature crude oils. Org. Geochem. 25, 179–190.

Cleaves, H.J., Jonsson, C.K., Jonsson, C.L., Sverjensky, D.A., Hazen, R.M., 2010. Adsorption of nucleic acid components on rutile (TiO_2) surfaces. Astrobio 10, 311–323.

Coleman, M.L., 1993. Microbial processes: controls on the shape and composition of carbonate concretions. Mar. Geol. 113, 127–140.

Coleman, M.L., Raiswell, R., 1995. Source of carbonate and origin of zonation in pyritiferous carbonate concretions: evaluation of a dynamic model. Am. J. Sci. 295, 282–308.

Condon, D., et al., 2005. U-Pb ages from the Neoproterozoic Doushantuo Formation, China. Science 308, 95–98.

Cook, P.J., Shergold, J.H., 1984. Phosphorus, phosphorites and skeletal evolution at the Precambrian-Cambrian boundary. Nature 308, 231–236.

Cotroneo, S., Schiffbauer, J.D., McCoy, V.E., Wortmann, U.G., Darroch, S.A.F., Peng, Y., Laflamme, M., 2016. A new model of the formation of Pennsylvanian iron carbonate concretions hosting exceptional soft-bodied fossils in Mazon Creek, Illinois. Geobiology 14, 543–555. https://doi.org/10.1111/gbi.12197.

Cui, H., Kitajima, K., Spicuzza, M.J., Fournelle, J.H., Denny, A., Iishida, A., Zhang, F., Valley, J.W., 2018. Questioning the biogenicity of Neoproterozoic superheavy pyrite by SIMS. Am. Minerol. 103, 1362–1400. https://doi.org/10.2138/am-2018-6489.

Dahanayake, K., Krumbein, W.E., 1986. Microbial structures in oolitic iron formations. Mineral. Deposita 21, 85–94.

Dahl, J.E., Moldowan, J.M., Peters, K.E., Claypool, G.E., Rooney, M.A., Michael, G.E., Mello, M.R., Kohnen, M.L., 1999. Diamondoid hydrocarbons as indicators of natural oil cracking. Nature 399, 54–57.

Dodd, M.S., Papineau, D., Grenne, T., Slack, J.F., Rittner, M., Pirajno, F., O'Neil, J., Little, C.T.S., 2017. Evidence for early life in Earth's oldest hydrothermal vent precipitates. Nature 543, 60–64. https://doi.org/10.1038/nature21377.

Dodd, M.S., Papineau, D., She, Z., Fogel, M., Nederbragt, S., Pirajno, F., 2018. Organic remains in late Palaeoproterozoic granular iron formations and implications for the origin of granules. Precambrian Res. 310, 133–152. https://doi.org/10.1016/j.precamres.2018.02.016.

Dodd, M.S., Shi, W., Li, C., Zhang, Z., Cheng, M., Gu, H., Hardisty, D.S., Loyd, S.J., Wallace, M.W., Hood, A.S., Lamothe, K., Mills, B.J.W., Poulton, S.W., Lyons, T.W., 2023. Uncovering the Ediacaran phosphorus cycle. Nature 618, 974–980. https://doi.org/10.1038/s41586-023-06077-6.

Duverger, A., Bernard, S., Viennet, J.-C., Miot, J., Busigny, V., 2021. Formation of pyrite spherules from mixtures of biogenic FeS and organic compounds during experimental diagenesis. Geochem. Geophys. Geosyst. 22, e2021GC010056. https://doi.org/10.1029/2021GC010056.

Elias, D.C., Mair, R.R., Mohiuddin, T.M.G., Morozov, S.V., Blake, P., Halsall, M.P., Ferrari, A.C., Boukhvalov, D.W., Katsnelson, M.I., Geim, A.K., Novoselov, K.S., 2009. Control of Graphene's properties by reversible hydrogenation: evidence for graphene. Science 343, 610–613.

Filik, J., 2006. Fundamental Studies on the Deposition and Characterisation of Novel Diamond-Like Materials. PhD thesis,. University of Bristol.
Fouke, B.W., 2011. Hot-spring systems geobiology: abiotic and biotic influences on travertine formation at Mammoth Hot Springs, Yellowstone National Park, USA. Sedimentology 58, 170–219.
Fujishima, A., Zhang, X., 2006. Titanium dioxide photocatalysis: present situation and future approaches. C.R. Chim. 9, 750–760.
Gabriel, N., Papineau, D., She, Z., Leider, A., Fogel, M.L., 2021. Organic diagenesis in stromatolitic dolomite and chert from the late Paleoproterozoic McLeary Formation. Precambrian Res. 354. https://doi.org/10.1016/j.precamres.2020.106052.
Goodwin, A., Papineau, D., 2022. Biosignatures associated with organic matter in late Paleoproterozoic stromatolitic dolomite and possible implications for Martian carbonates. Astrobiology 22, 1–27. https://doi.org/10.1089/ast.2021.0010.
Gorjan, P., Kaiho, K., Kakegawa, T., Niitsuma, S., Chen, Z.Q., Kajiwara, Y., Nicora, A., 2007. Paleoredox, biotic and sulfur-isotopic changes associated with the end-Permian mass extinction in the western Tethys. Chem. Geol. 244, 483–492. https://doi.org/10.1016/j.chemgeo.2007.07.003.
Götze, J., Möckel, R., Pan, Y., 2020. Mineralogy, geochemistry and genesis of agate—a review. Minerals 10, 1037–1088.
Grenne, T., Slack, J.F., 2003. Bedded jaspers of the Ordovician Løkken ophiolite, Norway: seafloor deposition and diagenetic maturation of hydrothermal plume-derived silica iron gels. Mineral. Deposita 38, 625–639.
Halverson, G.P., Hurtgen, M.T., 2007. Ediacaran growth of the marine sulfate reservoir. Earth Planet. Sci. Lett. 263, 32–44.
Hardisty, D.S., Lu, Z., Planavsky, N.J., Bekker, A., Philippot, P., Zhou, X., Lyons, T.W., 2014. An iodine record of Paleoproterozoic surface ocean oxygenation. Geology 42, 619–622.
Hartmnan, R.J., Kanning, E.W., Klee, F.G., 1934. The Liesegang phenomenon applied to banded malachite. J. Chem. Ed. 11, 346–350.
Heaney, P.J., Veblen, D.R., 1991. An examination of spherulitic dubiofossils in Precambrian banded iron formations using the transmission electron microscope. Precambrian Res. 49, 355–372.
Hiatt, E.E., Pufahl, P.K., Edwards, C.T., 2015. Sedimentary phosphate and associated fossil bacteria in a Paleoproterozoic tidal flat in the 1.85 Ga Michigamme Formation, Michigan, USA. Sediment. Geol. 319, 24–39. DOI: 10/1016/j.sedgeo.2015.01.006.
Huang, J., Chu, X., Lyons, T.W., Sun, T., Feng, L., Zhang, Q., Chang, H., 2013. The sulfur isotope signatures of Marinoan deglaciation captured in Neoproterozoic shallow-to-deep cap carbonate from South China. Precambrian Res. 238, 42–51.
Irwin, H., Curtis, C., Coleman, M., 1977. Isotopic evidence for source of diagenetic carbonates formed during burial of organic-rich sediments. Nature 269, 209–213.
Jamtveit, B., Hammer, Ø., 2012. Sculpting of rocks by reactive fluids. Geochem. Persp. 1, 341–480.
Jaszczak, J.A., Dimovski, S., Hackney, S.A., Robinson, G.W., Bosio, P., Gogotsi, Y., 2007. Micro- and nanoscale graphite cones and tubes from Hackman Valley, Kola Peninsula, Russia. Can. Mineral. 45, 379–389.
Jiang, G., Kennedy, M.J., Christie-Blick, N., 2003. Stable isotopic evidence for methane seeps in Neoproterozoic postglacial cap carbonates. Nature 426, 822–826.
Jiang, G., Kaufman, A.J., Christie-Blick, N., Zhang, S., Wu, H., 2007. Carbon isotope variability across the Ediacaran Yangtze platform in South China: Implications for a large surface-to-deep ocean $\delta^{13}C$ gradient. Earth Planet. Sci. Lett. 261, 303–320.
Jiang, G., Shi, X., Zhang, S., Wang, Y., Xiao, S., 2011. Stratigraphy and paleogeography of the Ediacaran Doushantuo Formation (ca. 635-551 Ma) in South China. Gondwana Res. 19, 831–849.
Jiao, L., She, Papineau, D., Zhang, C., Algeo, T.J., Dodd, M.S., Luo, G., Cao, K., Li, C., 2023a. Evidence for high-frequency oxygenation of Ediacaran shelf seafloor during early evolution of complex life. Commun. Earth Environ. 4. https://doi.org/10.1038/s43247-023-01080-1.
Jiao, L., She, Z., Papineau, D., Dodd, M.S., Zhang, Y., Cao, K., Du, Y., Chen, G., Chen, Q., Vickers-Rich, P., 2023b. Integrated stratigraphy and mineralogy of the Doushantuo Formation in Weng'an, South China and implications for Ediacaran phosphogenesis. J. Earth Sci. https://doi.org/10.1007/s12583-022-1765-3.
Köhler, I., Konhauser, K.O., Papineau, D., Bekker, A., Kappler, A., 2013. Biological carbon precursor to diagenetic siderite spherulites in banded iron formations. Nat. Commun. 4 (1741), 1–7. https://doi.org/10.1038/ncomms2770.
Konhauser, K.O., Lalonde, S.V., Planavsky, N.J., Pecoits, E., Lyons, T.W., Mojzsis, S.J., Rouxel, O.J., Barley, M.E., Rosiere, C., Fralick, P.W., Kump, L.R., Bekker, A., 2011. Aerobic bacterial pyrite oxidation and acid rock drainage during the Great Oxidation Event. Nature. https://doi.org/10.1038/nature10511.
Konhauser, K.O., Robbins, L.J., Alessi, D.S., Flynn, S.L., Gingras, M.K., Martinez, R.E., Kappler, A., Swanner, E.D., Li, Y.-L., Crowe, S.A., Planavsky, N.J., Reinhard, C.T., Lalonde, S.V., 2018. Phytoplankton contributions to the trace-element composition of Precambrian banded iron formations. GSA Bull. 130, 941–951.
Lan, Z., Sano, Y., Yahagi, T., Tanaka, K., Shirai, K., Papineau, D., Sawaki, Y., Ohno, T., Abe, M., Yang, H., Liu, H., Jiang, T., Wang, T., 2018. An integrated chemostratigraphic ($\delta^{13}C$- $\delta^{18}O$-$^{87}Sr/^{86}Sr$-$\delta^{15}N$) study of the Doushantuo Formation in western Hubei Province, South China. Precambrian Res. 320, 232–252. https://doi.org/10.1016/j.precamres.2018.10.018.
Leri, A.C., Hakala, A., Marcus, M.A., Lanzarotti, A., Reddy, C.M., Myneni, S.C.B., 2010. Natural organobromine in marine sediments: new evidence of biogeochemical Br cycling. Glob. Biogeochem. Cycles 24. https://doi.org/10.1029/2010GB003794.
Li, C., Love, G.D., Lyons, T.W., Fike, D.A., Sessions, A.L., Chu, X., 2010. A stratified redox model for the Ediacaran Ocean. Science 328, 80–83.
Liesegang, R.E., 1910. Die Entstehung der Achate. Zentralbl. Mineral. 11, 593–597.
Liu, D., Yu, N., Papineau, D., Fan, Q., Wang, H., Qiu, X., She, Z., Luo, G., 2019. The catalytic role of planktonic aerobic heterotrophic bacteria in protodolomite formation: results from Lake Jibuhulangtu Nuur, Inner Mongolia, China. Geochim. Cosmochim. Acta 263, 31–49. https://doi.org/10.1016/j.gca.2019.07.056.
Lougheed, M.S., 1983. Origin of Precambrian iron-formations in the Lake Superior region. Geol. Soc. Am. Bull. 94, 325–340.
Maliva, R.G., Knoll, A.H., Simonson, B.M., 2005. Secular change in the Precambrian silica cycle: insights from chert petrology. GSA Bull. 115, 835–845. https://doi.org/10.1130/B25555.1.
Marshall, J.D., Pirrie, D., 2013. Carbonate concretions – explained. Geol. Today 29, 53–62.
McFadden, K., Huang, J., Chu, X., Jiang, G., Kaufman, A.J., Zhou, C., Yuan, X., Xiao, S., 2008. Pulsed oxidation and biological evolution in the Ediacaran Doushantuo Formation. Proc. Natl. Acad. Sci. 105, 3197–3202.
Moczydłowska, M., Liu, P., 2021. Ediacaran algal cysts from the Doushantuo Formation, South China. Geol. Mag. https://doi.org/10.1017/S0016756820001405.
Mossman, D.J., Gauthier-Lafaye, F., Jackson, S.E., 2005. Black shales, organic matter, ore genesis and hydrocarbon generation in the Paleoproterozoic Franceville Series, Gabon. Precambrian Res. 137, 253–272.
Muscente, A.D., Hawkins, A.D., Xiao, S., 2015. Fossil preservation through phosphatization and silicification in the Ediacaran Doushantuo Formation (South China): a comparative synthesis. Palaeogeogr. Palaeoclimatol. Palaeoecol. 434, 46–62.
Oertel, G., Curtis, C.D., 1972. Clay-ironstone concretion preserving fabrics due to progressive compaction. Geol. Soc. Am. Bull. 83, 2597–2606.
Ohfuji, H., Rickard, D., 2005. Experimental syntheses of framboids – a review. Earth Sci. Rev. 71, 147–170. https://doi.org/10.1016/j.earthscirev.2005.02.001.
Papineau, D., 2020. Chemically oscillating reactions in the formation of botryoidal malachite. Am. Minerol. 105, 447–454. https://doi.org/10.2138/am-2019-7029.
Papineau, D., 2024. Chemically oscillating reactions as a new model for the formation of mineral patterns in agate geodes and concretions. Minerals 14. https://doi.org/10.3390/min14020203.
Papineau, D., De Gregorio, B.T., Fearn, S., Kilcoyne, D., Purohit, R., Fogel, M.L., 2016. Nanoscale petrographic and geochemical insights on the origin of Paleoproterozoic stromatolitic phosphorites from Aravalli, India. Geobiology. https://doi.org/10.1111/gbi12164.
Papineau, D., She, Z., Dodd, M.S., 2017. Chemically oscillating reactions during the diagenetic oxidation of organic matter and in the formation of granules in late Paleoproterozoic chert from Lake Superior. Chem. Geol. 470, 33–54. https://doi.org/10.1016//j.chemgeo.2017.08.021.
Papineau, D., Yin, J., Devine, K., Liu, D., She, Z., 2021. Chemically oscillating reactions during the diagenetic formation of Ediacaran siliceous and carbonate botryoids. Minerals 11, 1–30. https://doi.org/10.3390/min11101060.
Papineau, D., Dodd, M.S., She, Z., Iacoviello, F., Hauri, E., Shearing, P., Little, C.S., 2022. Metabolically diverse primordial microbial communities in Earth's oldest seafloor-hydrothermal jasper. Sci. Adv. 70. https://doi.org/10.1126/sciadv.abm2296.
Papineau, D., Devine, K., Albuquerque Nogueira, B., 2023. Self-similar patterns from abiotic decarboxylation metabolism through chemically oscillating reactions: a prebiotic model for the origin of life. Life. https://doi.org/10.3390/life13020551.
Pecoits, E., Gingras, M.K., Barley, M.E., Kappler, A., Potsh, N.R., Konhauser, K.O., 2009. Petrography and geochemistry of the Dales Gorges banded iron formation: paragenetic sequence, source, and implications for palaeo-ocean chemistry. Precambrian Res. 172, 163–172.
Plet, C., Grice, K., Pages, A., Ruebsam, W., Coolen, M.J.L., Schwark, L., 2016. Microbially-mediated fossil-bearing carbonate concretions and their significance for paleoenvironmental reconstructions: a multi-proxy organic and inorganic geochemical appraisal. Chem. Geol. 426, 95–108. https://doi.org/10.1016/j.chemgeo.2016.01.026.
Pufahl, P.K., Grimm, K.A., 2003. Coated phosphate grains: proxy for physical chemical and ecological changes in seawater. Geology 31, 801–804.
Rassmusen, B., Meier, D.B., Krapez, B., Mulhing, J.R., 2013. Iron silicate microgranules as precursor sediments to 2.5-billion-year-old banded iron formations. Geology 41, 435–438. https://doi.org/10.1130/G33828.1.
Rogov, M., Ershova, V., Vereshchagin, O., Vasileva, K., Mikhailova, K., Krylov, A., 2021. Database of global glendonite and ikaite records throughout the Phanerozoic. Earth Sys. Sci. Data 13, 343–356. https://doi.org/10.5194/essd-13-343-2021.
Sánchez-Román, M., Fernandez-Remolar, D., Amils, R., Sanchez-Navas, A., Schmid, T., Martin-Uriz, P.S., Rodriguez, N., McKenzie, J.A., Vasconcelos, C., 2014. Microbial mediated formation of Fe-carbonate minerals under extreme acidic conditions. Sci. Rep. https://doi.org/10.1038/srep04767.
Schieber, J., 2007. Oxidation of detrital pyrite as a cause for marcasite formation in marine lag deposits from the Devonian of the eastern US. Deep-Sea Res. II (54), 1312–1326. https://doi.org/10.1016/j.dsr2.2007.04.005.
Schopf, J.W., Kudryavtsev, A.B., 2012. Biogenecity of Earth's earliest fossils: a resolution of the controversy. Gondwana Res. 22, 761–771. https://doi.org/10.1016/j.gr.2012.07.003.
Schwid, M.F., Xiao, S., Nola, M., An, Z., 2021. Differential weathering of diagenetic concretions and the formation of Neoproterozoic annulated discoidal structures. Palaios 36, 15–27. https://doi.org/10.2110/palo.2020.018.
Seilacher, A., 2001. Concretion morphologies reflecting diagenetic and epigenetic pathways. Sediment. Geol. 143, 41–57.
She, Z., Strother, P., McMahon, G., Nittler, L.R., Wang, J., Zhang, J., Longkang, S., Ma, C., Papineau, D., 2013. Terminal Proterozoic cyanobacterial blooms and phosphogenesis documented by the Doushantuo granular phosphorites I: *in situ* micro-analyses of textures and composition. Precambrian Res. 235, 20–35.
She, Z., Strother, P., Papineau, D., 2014. Terminal Proterozoic cyanobacterial blooms and phosphogenesis documented by the Doushantuo granular phosphorites II: petrology and carbon isotopes. Precambrian Res. 251, 62–79.

She, Z.-B., Zhang, Y.-T., Liu, W., Song, J., Zhang, Y., Li, C., Strother, P., Papineau, D., 2016. New observations of ambient inclusion trails (AITs) and pyrite framboids in the Ediacaran Doushantuo Formation, South China. Palaeogeogr. Palaeoclimatol. Palaeoecol. 461, 374–388.
Shields, G.A., Webb, G.E., 2004. Has the REE composition of seawater changed over geological time? Chem. Geol. 204, 103–107.
Simonson, B.M., 1985. Sedimentology of cherts in the Early Proterozoic Wishart Formation, Quebec-Newfoundland, Canada. Sedimentology 32, 23–40.
Sirantoine, E., Wacey, D., Bischoff, K., Saunders, M., 2020. Authigenic anatase within 1 billion-year-old cells. Geobiology 1–15. https://doi.org/10.1111/gbi.12417.
Stefurak, E.J.T., Lowe, D.R., Zentner, D., Fischer, W.W., 2015. Sedimentology and geochemistry of Archean silica granules. Geol. Soc. Am. Bull. 127, 1090–1107. https://doi.org/10.1130/B31181.1.
Tan, P.H., Hu, C.Y., Dong, J., Shen, W.C., Zhang, B.F., 2001. Polarization properties, high-order Raman spectra, and frequency asymmetry between Stokes and anti-Stokes scattering of Raman modes in a graphite whisker. Phys. Rev. B 64. https://doi.org/10.1103/PhysRevB.64.214301.
Tan, P.H., An, L., Liu, L.Q., Guo, Z.X., Czerw, R., Carroll, D.L., Ajayan, P.M., Zhang, N., Guo, H.L., 2002. Probing the phonon dispersion relations of graphite from the double-resonance process of Stokes and anti-Stokes scatterings in multiwalled carbon nanotubes. Phys. Rev. B 64. https://doi.org/10.1103/PhysRevB.66.245410.
Truong, C., Bernard, S., Le Pape, P., Morin, G., Baya, C., Merrot, P., Gorlas, A., Guyot, F., 2023. Production of carbon-containing spherules induced by hyperthermophilic Thermococcales: a biosignature? Front. Microbiol. 14, 1145781. https://doi.org/10.3389/fmicb.2023.1145781.
Varkouhi, S., Papineau, D., 2023. Silica botryoids from chemically oscillating reactions and as Precambrian environmental proxies. Geology. https://doi.org/10.1130/G50948.1.
Varkouhi, S., Papineau, D., Guo, Z., 2022. Botryoidal quartz as an abiotic signature in Palaeoarchean cherts of the Pilbara Supergroup, Western Australia. Precambrian Res. https://doi.org/10.1016/j.precamres.2022.106876.
Wacey, D., Kilburn, M.R., Saunders, M., Cliff, J.B., Kong, C., Liu, A.G., Matthews, J.J., Brasier, M.D., 2014. Uncovering framboidal pyrite biogenicity using nano-scale CN_{org} mapping. Geology 43, 27–30. https://doi.org/10.1130/G36048.1.
Walter, M.R., Goode, A.D.T., Hall, W.D.M., 1976. Microfossils from a newly discovered Precambrian stromatolitic iron formation in Western Australia. Nature 261, 221–223.
Wang, J., Jiang, G., Xiao, S., Li, Q., Wei, Q., 2008. Carbon isotope evidence for widespread methane seeps in the ca. 635 Ma Doushantuo cap carbonate in South China. Geology 36, 347–350.
Wang, Z., Wang, J., Suess, E., Wang, G., Chen, C., Xiao, S., 2017. Silicified glendonites in the Ediacaran Doushantuo Formation (South China) and their potential paleoclimatic implications. Geology 45, 115–118.
Wang, X., Jiang, G., Xiaoying, S., Peng, Y., Morales, D.C., 2018. Nitrogen isotope constraints on the early Ediacaran Ocean redox structure. Geochim. Cosmochim. Acta 240, 220–235. https://doi.org/10.1016/j.gca.2018.08.034.
Wang, Z., Chen, C., Wang, J., Suess, E., Chen, X., Ma, X., Wang, G., Xiao, S., 2020. Wide but not ubiquitous distribution of glendonite in the Doushantuo Formation, South China: implications for Ediacaran climate. Precambrian Res. 338. https://doi.org/10.1016/j.precamres.2019.105586.
Wang, H., Peng, Y., Li, C., Cao, X., Cheng, M., Bao, H., 2023. Sulfate triple-oxygen-isotope evidence confirms oceanic oxygenation 570 million years ago. Nat. Commun. 14, 4315. https://doi.org/10.1038/s41467-023-39962-9.
Wei, H., Wang, X., Shi, X., Jiang, G., Tang, D., Wang, L., An, Z., 2019. Iodine content of the carbonates from the Doushantuo Formation and shallow ocean redox change on the Ediacaran Yangtze Platform, South China. Precambrian Res. 322, 160–169.
Wignall, P.B., Newton, R., 1998. Pyrite framboid diameter as a measure of oxygen deficiency in ancient mudrocks. Am. J. Sci. 298, 537–552.
Wilkin, R.T., Barnes, H.L., Brantley, S.L., 1996. The size distribution of framboidal pyrite in modern sediments: an indicator of redox conditions. Geochim. Cosmochim. Acta 60, 3897–3912.
Wilson, D.D., Brett, C.E., 2013. Concretions as sources of exceptional preservation, and decay as a source of concretions: examples from the Middle Devonian of New York. Palaios 28, 305–316. https://doi.org/10.2110/palo.2012.p12-086r.
Xiao, S., Zhang, Y., Knoll, A.H., 1998. Three-dimensional preservation of algae and animal embryos in a Neoproterozoic phosphorite. Nature 391, 553–558.
Xiao, S., Schiffbauer, J.D., McFadden, K.A., Hunter, J., 2010. Petrographic and SIMS pyrite sulfur isotope analyses of Ediacaran chert nodules: implications for microbial processes in pyrite rim formation, silicification, and exceptional fossil preservation. Earth Planet. Sci. Lett. 297, 481–495.
Xiao, S., Zhou, C., Liu, P., Wang, D., Yuan, X., 2014. Phosphatized acanthomorphic acritarchs and related microfossils from the Ediacaran Doushantuo formation at Weng'an (South China) and their implications for biostratigraphic correlation. J. Paleontol. 88, 1–67. https://doi.org/10.1666/12-157R.
Yang, C., Rooney, A.D., Condon, D.J., Li, X.-H., Grazhdankin, D.V., Bowyer, F.T., Hu, C., Macdonald, F.A., Zhu, M., 2021. The tempo of Ediacaran evolution. Sci. Adv. 7.
Yang, H., Chen, Z.-Q., Papineau, D., 2022. Biosignatures in microdigitate stromatolites from the Mesoproterozoic Wumishan Formation, Jixian, North China. Precambrian Res. 368. https://doi.org/10.1016/j.precamres.2021.106496.
Zaikin, A.N., Zhabotinsky, A.M., 1970. Concentration wave propagation in two-dimensional liquid-phase self-oscillating system. Nature 225, 535–537.
Zhou, C., Xiao, S., 2007. Ediacaran $\delta^{13}C$ chemostratigraphy of South China. Chem. Geol. 237, 89–108. https://doi.org/10.1016/j.chemgeol.2006.06.021.
Zhu, M., Lu, M., Zhang, J., Zhao, F., Li, G., Aihua, Y., Zhao, X., Zhao, M., 2013. Carbon isotope chemostratigraphy and sedimentary facies evolution of the Ediacaran Doushantuo Formation in western Hubei, South China. Precambrian Res. 225, 7–28.